HER2 heterogeneous breast cancer models reveal novel therapeutic targets and subclonal dynamics during evolution to resistance to HER2-targeted therapies

Marie-Anne Goyette[1,2,3], Christopher Graser[4,5,6], Marco Seehawer[1,2,3], Andriana Patmanidis[1], Ernesto Rojas Jimenez[1,2,3], Avni Kamat[1], Pengze Yan[1,2,3], Anne Fassl[7,8], Pierre Foidart[1,2,3], Zheqi Li[1,2,3], Ameera James[1], George Sflomos[9], Cathrin Brisken[9,10], Piotr Sicinski[5,6], Franziska Michor[4,5,6,11,12,13] and Kornelia Polyak[1,2,3,11,12,13]

[1]Department of Medical Oncology, Dana-Farber Cancer Institute, Boston, MA 02215, USA.
[2]Department of Medicine, Harvard Medical School, Boston, MA 02115, USA.
[3]Department of Medicine, Brigham and Women's Hospital, Boston, MA 02115, USA.
[4]Department of Data Science, Dana-Farber Cancer Institute, Boston, MA 02215, USA.
[5]Department of Biostatistics, Harvard T.H. Chan School of Public Health, Boston, MA 02115, USA.
[6]Department of Stem Cell and Regenerative Biology, Harvard University, Cambridge, MA 02138, USA.
[7]Department of Cancer Biology, Dana-Farber Cancer Institute, Boston, MA 02215, USA.
[8]Department of Genetics, Blavatnik Institute, Harvard Medical School, Boston, MA 02115, USA.
[9]Swiss Institute for Experimental Cancer Research, School of Life Sciences, Ecole Polytechnique Fédérale de Lausanne (EPFL), CH-1015, Lausanne, Switzerland.
[10]Breast Cancer Now Research Centre, Institute of Cancer Research, London, UK.
[11]The Broad Institute of MIT and Harvard, Cambridge, MA 02142, USA.
[12]The Ludwig Center at Harvard, Boston, MA 02115, USA.
[13]The Center for Cancer Evolution, Dana-Farber Cancer Institute, Boston, MA 02215, USA.

Running title: Preclinical models of HER2 heterogeneous breast cancer

Correspondence and requests for materials should be addressed to Kornelia Polyak, Dana-Farber Cancer Institute, 450 Brookline Ave., Boston, MA 02215, 617-632-2106, kornelia_polyak@dfci.harvard.edu

AUTHOR'S DISCLOSURES

K. Polyak serves on the Scientific Advisory Board of Ideaya Biosciences, is an adviser to Curie.Bio, holds equity in Antares Therapeutics and stock options in Ideaya Biosciences, receives funding from Novartis, and honoraria from Astra-Zeneca, and Novartis, and payment from ELI Lilly for Scorpion Biosciences stock sale in the past 24 months. **P. Sicinski** has been a consultant at Novartis, Genovis, Guidepoint, The Planning Shop, ORIC Pharmaceuticals, Cedilla Therapeutics, Syros Pharmaceuticals, Blueprint Medicines, Curie Bio, Differentiated Therapeutics, Excientia, Ligature Therapeutics, Merck, Redesign Science, Scorpion Therapeutics, Incyte, Serinus Biosciences, Sibylla Biotech, and Exo Therapeutics, and received sponsored research funding from Novartis. The other authors declare no competing interests. **K. Polyak** and **M.-A. Goyette** are inventors of a patent application based on the data presented in this manuscript.

ABSTRACT

Intratumor heterogeneity for HER2 in HER2-positive breast cancer is a driver of resistance to HER2-targeted therapies. The advancement of treatments for HER2 heterogeneous tumors has been hindered by the lack of preclinical models that accurately mimic the human disease. Here we describe human HER2 heterogeneous breast cancer models composed of *ERBB2* amplified ($HER2^{hi}$) and non-amplified ($HER2^{lo}$) cell populations derived from the same tumor. Utilizing these models, together with cellular barcoding, we demonstrate subclonal cooperation between $HER2^{hi}$ and $HER2^{lo}$ subpopulations. Furthermore, $HER2^{lo}$ cells drive resistance to HER2-targeting antibody-drug conjugates (ADC) like T-DXd but are sensitive to HER2 kinase inhibitors. CRISPR screens in heterogeneous co-cultures identified sensitizers of $HER2^{lo}$ cells to T-DXd including ABCC1 and USP9X. USP9X inhibition enhances the lysosomal targeting of HER2, thereby potentiating ADC payload release and reducing tumor recurrence after T-DXd treatment. Our results elucidate the functional relevance of HER2 heterogeneity and propose improved therapies for these tumors.

Keywords: Breast cancer; HER2; Heterogeneity; T-DXd

STATEMENT OF SIGNIFICANCE

Studies of HER2 heterogeneous breast cancer models demonstrated that $HER2^{lo}$ cells drive HER2-targeting ADC resistance and accelerate recurrence by cooperating with $HER2^{hi}$ cells. We identified novel therapeutic strategies to sensitize $HER2^{lo}$ cells to T-DXd, providing mechanistic insight and offering promising avenues to overcome resistance and improve patient outcomes.

INTRODUCTION

HER2-positive breast cancer, which accounts for approximately 20% of breast cancer cases, is characterized by the amplification and overexpression of the human epidermal growth factor receptor 2 (HER2), encoded by the *ERBB2* gene (1,2). The development of HER2-targeted treatment strategies has revolutionized the management of the disease, leading to substantial improvements in patient outcomes (3,4). Currently used HER2-targeting therapies include monoclonal antibodies (e.g., trastuzumab, pertuzumab), small-molecule inhibitors (e.g., tucatinib, neratinib, lapatinib), and, more recently, antibody–drug conjugates (ADCs) such as T-DM1 and T-DXd (5,6). These ADCs, which link trastuzumab to cytotoxic agents, are particularly promising, as they bind to target-expressing cells, trigger receptor-mediated internalization, and release their payload mainly through lysosomal cleavage of the linker, resulting in targeted cell death (7,8). However, despite these advances, treatment resistance remains a major clinical challenge.

Intratumoral heterogeneity for HER2 has emerged as a critical resistance mechanism to HER2-targeted therapies, including ADCs (9-12). HER2 heterogeneous breast cancer, defined by the American Society of Clinical Oncology (ASCO)/College of American Pathologists (CAP) guidelines as the presence of *ERBB2* amplification in more than 5% but less than 50% of cancer cells, or a HER2-negative area by Fluorescence In Situ Hybridization (FISH) (13,14), represents up to 40% of HER2+ breast cancer cases. Patients with HER2 heterogeneous tumors have shorter survival in both early and advanced-stage disease (10-12). We previously reported in the NCT02326974 clinical trial that the presence of *ERBB2* non-amplified cells in pre-treatment tumors is associated with the lack of pathological complete response (pCR) to the neoadjuvant pertuzumab and T-DM1 combination, where none of the patients with HER2-heterogeneous tumors achieved pCR, while over half of those with non-heterogeneous tumors did (9). It remains to be tested whether similar observations hold for T-DXd which has a cleavable linker and a membrane-permeable payload, enabling a bystander effect allowing for the killing of nearby cells even if they lack HER2 (15). However, our follow up characterization of the gene expression

profiles of pre-/post-treatment tumors from the NCT02326974 trial revealed almost complete lack of transcriptional response to pertuzumab and T-DM1 treatment in HER2 heterogeneous tumors despite high inferred activity of the HER2 signaling pathway, implying important biological differences beyond HER2 (16). Despite this compelling data, HER2 heterogeneity is still not considered in clinical decision-making and therapeutic strategies tailored for these patients are lacking. Therefore, investigation of the biology and vulnerabilities of HER2 heterogeneous tumors is crucial for developing more effective therapies, which requires preclinical models that faithfully reproduce the disease.

Here we describe the generation and characterization of HER2 heterogeneous breast cancer models that recapitulate human tumors. We leveraged these models to investigate the functional relevance of HER2 heterogeneity by following subclonal dynamics during the evolution of resistance to HER2-targeted therapies and performing CRISPR screens to identify novel therapeutic vulnerabilities.

RESULTS

Generation and characterization of HER2 heterogeneous breast cancer models

To assess intratumoral heterogeneity for HER2, we performed flow cytometry for cell surface HER2 in a panel of human HER2+ breast cancer cell lines (**Fig. 1A**). We observed the highest fraction of $HER2^{lo}$ cells in the 21PT, 21NT, and HCC1954 cell lines at 29.4%, 10.9% and 14.3%, respectively (**Fig. 1A**). 21NT and 21PT are two cell lines with distinct phenotypes and genotypes derived from the same primary tumor of a patient with an aggressive HER2+ breast cancer resistant to chemotherapy (17), while the HCC1954 line was derived from a high-grade HER2+ breast cancer following radiation treatment (18). To isolate $HER2^{hi}$ and $HER2^{lo}$ subpopulations, we sorted and then regrew the cells, repeating the process a total of five times. The isolated $HER2^{hi}$ and $HER2^{lo}$ populations maintained their HER2 expression levels even after more than 10 passages (**Fig. 1B** and **1C**), and their identity was confirmed by short tandem repeat (STR) profiling (**Supplementary Table S1**).

Next, we performed FISH to assess *ERBB2* copy number and observed *ERBB2* amplification in $HER2^{hi}$ but not in $HER2^{lo}$ cells, consistent with the clinical definition of HER2 heterogeneous tumors (**Fig. 1D**). We investigated additional genetic differences between paired $HER2^{hi}$ and $HER2^{lo}$ subsets from the same cell line by whole exome sequencing (WES), which revealed largely overlapping copy number variation (CNV) except for the *ERBB2* amplicon (**Fig. 1E**, **Supplementary Table S2**). Additionally, analysis of the single nucleotide variants (SNV) revealed both shared and distinct mutations between $HER2^{hi}$ and $HER2^{lo}$ cells in tumor suppressor and oncogenes that are mutated in breast cancer according to the TCGA cohort (**Fig. 1F**). The p.R816H *ERBB2* mutation detected in the $HER2^{hi}$ population of the 21NT and 21PT cell lines is not known to be oncogenic and it is potentially neutral. Overall, multiple SNVs were shared between the matched populations at comparable allelic frequencies suggesting that $HER2^{hi}$ and $HER2^{lo}$ cell populations within the same tumor have a common clonal origin (**Supplementary Fig. S1A** and **Supplementary Table S2**). However, no mutations were shared between all $HER2^{lo}$ cells from the

different cell lines indicating that HER2 heterogeneous tumors are not driven by recurrent mutations. Conversely, genes specifically mutated in HER2^{lo} cells included pathways linked with growth factor (e.g. IGF and PDGF) and PI3K signaling that drive cell proliferation, survival, and oncogenic transformation in cancer (**Supplementary Fig. S1B**).

To characterize differences between HER2^{hi} and HER2^{lo} cells at the single cell level, including signaling pathway activity, we performed cytometry by time of flight (CYTOF) analysis. HER2 was the most consistently differentially expressed protein with high expression in HER2^{hi} cells in both models, while markers of cell proliferation (e.g., CDK1) and cell state (e.g., CD49F, CD24) showed more subtle and less consistent differences (**Supplementary Fig. S1C**). HER2 interacting proteins (HER3 and EGFR) did not show clear differences between HER2^{hi} and HER2^{lo} cells, while HER2^{lo} cells had slightly lower levels of downstream components of the HER2 signaling pathway (phospho-AKT and phospho-S6).

We next utilized RNA-sequencing to further characterize these cells and determined that the main difference between HER2^{hi} and HER2^{lo} cells was the expression of genes located in the *ERBB2* amplicon (**Supplementary Fig. S1D**). There was a small overlap in the differentially expressed genes between HER2^{hi} and HER2^{lo} cells from different lines, and no clear clustering of the samples based on the differentially expressed genes, suggesting HER2^{hi} and HER2^{lo} cells from different tumors have little in common (**Supplementary Fig. S1E** and **S1F**). Analysis of signaling pathway activity using Gene Set Enrichment Analysis (GSEA) also did not show consistent pathway differences between HER2^{hi} and HER2^{lo} cells across cell lines (**Supplementary Fig. S1G** and **S1H**, **Supplementary Table S3**). However, PAM50 subtype (19) probability predictions consistently showed that HER2^{lo} cells are less HER2-like and more basal compared to their HER2^{hi} counterparts (**Fig. 1G**). This observation is in agreement with our data from the NCT02326974 clinical trial demonstrating that treatment-naïve HER2 heterogeneous tumors are transcriptionally more basal than HER2 non-heterogeneous tumors (16). To extend these findings, we re-analyzed our cyclic immunofluorescence (CycIF) data obtained from a subset of treatment-

naïve HER2+ tumors in the NCT02326974 trial (20), focusing on cells with high versus low HER2 expression. Consistent with the PAM50 prediction scores above, $HER2^{lo}$ cells from those patient tumors had higher levels of basal (CK5 and CK14) and mesenchymal (vimentin) but lower expression of luminal (CK19, CK7 or CK8) markers (**Fig. 1H**).

Overall, these data demonstrate that the HER2 heterogeneous cell line models we generated accurately reflect the genetic and transcriptomic features of HER2 heterogeneous breast cancer.

$HER2^{lo}$ cells are resistant to HER2-targeting ADCs

To facilitate the tracking of $HER2^{hi}$ and $HER2^{lo}$ cells in live cultures, we marked them with H2B-mcherry ($HER2^{hi}$ cells) and H2B-GFP ($HER2^{lo}$ cells) using lentiviral transduction. We then assessed the response of these $HER2^{hi}$ and $HER2^{lo}$ subpopulations as well as parental cell lines to HER2-targeting agents including ADCs (trastuzumab deruxtecan, T-DXd and trastuzumab emtansine, T-DM1) and HER2 tyrosine kinase inhibitors (TKIs) (neratinib and tucatinib). $HER2^{lo}$ cells showed reduced sensitivity to ADCs but not to HER2 TKIs compared to corresponding $HER2^{hi}$ and parental cells (**Fig. 2A, Supplementary Fig. S2A** and **S2B**). Tucatinib, a HER2-specific TKI, was slightly less effective than neratinib in 21PT cells, thus, we also tested two additional HER2-specific inhibitors (zongertinib and CP-724714) but did not observe significant differences between $HER2^{hi}$ and $HER2^{lo}$ cells in either model (**Fig. 2A, Supplementary Fig. S2C** and **S2D**). The difference in response between $HER2^{hi}$ and $HER2^{lo}$ cells to T-DXd was less pronounced in the 21NT line but this was not the case in the HCC1954 model. The response of 21NT and 21PT $HER2^{lo}$ cells to HER2-targeting ADCs was comparable to that of MDA-MB-468 basal and MDA-MB-231 mesenchymal triple-negative breast cancer (TNBC) cell lines lacking HER2, while HCC1954 $HER2^{lo}$ cells were more sensitive than TNBC cells, consistent with their higher level on HER2 (**Supplementary Fig. S2E** and **S2F**). Sensitivity to chemotherapeutic agents like paclitaxel and 5-fluorouracil (5-FU), and deruxtecan (DXd), the payload of T-DXd, did not show significant

differences indicating that the reduced response of HER2^{lo} cells to T-DXd is not due to the payload or general chemoresistance (**Supplementary Fig. S2G**). Furthermore, immunoblot analysis of downstream components of the EGFR/HER2 signaling pathway demonstrated baseline differences between HER2^{hi} and HER2^{lo} populations, but both showed a pronounced decrease following neratinib treatment, in line with our observation (**Fig. 2B**).

We next performed cellular competition experiments by treating a 1:1 mixture of HER2^{hi} and HER2^{lo} cell cultures with HER2-targeting ADCs or TKIs. Using these assays, we found that HER2^{lo} cells dominated the population after 10 passages of ADC but not TKI treatment (**Supplementary Fig. S2H**). This finding was observed in the HCC1954 and 21NT but not in the 21PT model, likely due to the higher sensitivity of 21PT HER2^{hi} cells to TKIs compared to their HER2^{lo} counterparts (**Supplementary Fig. S2B**). To validate our results in clinical samples, we performed single-cell RNA-seq (scRNA-seq) on two HER2+ tumors (T537 and T565) and also generated patient-derived organoids (PDOs) from them. Both the scRNA-seq data on the clinical samples and flow cytometry on the PDOs confirmed the presence of HER2^{hi} and HER2^{lo} cancer cell subpopulations (**Fig. 2C Supplementary Fig. S2I** and **S2J**). We treated these PDOs with T-DXd or neratinib for 2 weeks and observed an increase in the relative fraction of the HER2^{lo} subpopulation, confirming that HER2^{lo} cells are less sensitive to HER2-targeting agents (**Fig. 2C** and **Supplementary Fig. S2J**). This observation was also validated in a patient-derived xenograft (PDX, Mets15) cultured as organoids (**Supplementary Fig. S2J**).

To further investigate the dynamics of HER2^{hi} and HER2^{lo} cell populations and mechanisms of resistance to HER2-targeting agents in our models, we generated resistant derivatives of each of the three parental cell lines to all four agents by prolonged culture in the presence of the drug. We first assessed *ERBB2* copy numbers by FISH, which revealed selection for *ERBB2* non-amplified cells in T-DXd (TDR) and T-DM1 (TMR) resistant derivates, whereas neratinib (NR) and tucatinib (TR) resistant cells still showed the same level of *ERBB2* amplification as cells passaged in vehicle for the same time (Ctl) (**Fig. 2D** and **Supplementary Fig. S3A**). Accordingly, analysis of

RNA-seq data demonstrated that TDR and TMR cells clustered more closely with corresponding HER2^{lo} cells, based on Euclidean distance in a principal component analysis (PCA), while HER2^{hi} cells showed similar distance from all resistant derivates (**Fig. 2E** and **2F, Supplementary Fig. S3B**). Apoptosis and TGF-β signaling were specifically enriched in TDR and TMR, respectively, compared to HER2^{lo} cells, suggesting that selection for *ERBB2* non-amplified cells is not the only feature of resistance to these ADCs (**Supplementary Fig. S3C**). Furthermore, GSEA across all three models showed differences between ADC and TKI resistant derivates in E2F and MYC targets (**Supplementary Fig. S3D** and **Supplementary Table S4**). Immunoblot analysis of parental and resistant cells at baseline for HER2/EGFR signaling pathway components identified a decrease in HER2 itself as the main distinguishing feature of ADC-resistant cells (**Supplementary Fig. S3E**). We also investigated cross-resistance across the four agents and found that TDR and TMR cells were resistant to both ADCs but still sensitive to TKIs whereas NR and TR cells were resistant to both TKIs but sensitive to T-DXd and T-DM1 (**Fig. 2G, Supplementary Fig. S3F**).

To investigate potential drivers of resistance in these lines, we analyzed correlations between the half maximal inhibitory concentration (IC50) values of the four HER2-targeting agents and the proportion of HER2^{lo} cells across a panel of HER2+ breast cancer cell lines, finding significant positive correlation between HER2^{lo} cells proportions and the IC50 to T-DXd and T-DM1 (**Supplementary Fig. S3G**). Tucatinib, which exhibits greater specificity for HER2, demonstrated a trend similar to that of the ADCs, but not the pan-HER inhibitor neratinib. Given these observations, we next tested whether combining ADCs with neratinib would more effectively inhibit HER2 heterogeneous cultures. We found that the combination of neratinib and T-DXd was more effective than either agent alone in all three parental cell lines (**Supplementary Fig. S3H**), in line with prior cell culture and clinical data (21,22), supporting this approach as a potential strategy for HER2 heterogeneous tumors.

HER2^{hi} and HER2^{lo} cells cooperate in co-culture

HER2^{lo} cells were a minor subpopulation and slower growing compared to HER2^{hi} cells in each of the three parental lines (**Fig. 1A**); thus, their persistence raised the possibility of subclonal cooperation between HER2^{hi} and HER2^{lo} cells. To test this hypothesis, we compared the growth of HER2^{hi} and HER2^{lo} cells when cultured alone (monoculture) and in 1:1 co-culture. We observed that in control conditions, both HER2^{hi} and HER2^{lo} cells grew faster in co-culture compared to monoculture (**Fig. 3A, Supplementary Fig. S4A** and **S4B**). To further study the interaction between HER2^{hi} and HER2^{lo} cells in vitro, we conducted RNA-seq analysis on sorted cells from monoculture and co-culture. GSEA revealed that genes related to epithelial-to-mesenchymal transition (EMT) were commonly upregulated in the co-cultures across cell lines (**Supplementary Fig. S4C** and **Supplementary Table S5**). Additionally, Reverse Phase Protein Array (RPPA) revealed a decrease of E-cadherin in co-culture of 21PT as one of the most differentially present proteins in this condition (**Supplementary Fig. S4D** and **Supplementary Table S6**). In HCC1954, co-culture increased the expression of immune checkpoint proteins B7-H3 and PD-L1. A cytokine array also showed an increase of angiogenesis related factors in co-culture of HCC1954 (**Supplementary Fig. S4E**). Even though the two cell lines show differences the pathways regulated, these data suggest enhanced plasticity and adaptation when HER2^{hi} and HER2^{lo} cells are interacting in co-culture.

Interestingly, the response of HER2^{hi} or HER2^{lo} cells to HER2-targeting agents was the same in monoculture and co-culture (**Fig. 3A, Supplementary Fig.S4A** and **S4B**). T-DXd has been proposed to have a bystander effect (15), however, in our models HER2^{lo} cells did not show increased sensitivity to T-DXd when co-cultured with HER2^{hi} cells (**Fig. 3A, Supplementary Fig. S3A** and **S3B**). To further investigate the bystander effect of T-DXd, we tested the same cell lines (MDA-MB-468 basal TNBC and KPL4 HER2+ inflammatory breast cancer cells) used in the original paper describing the T-DXd bystander effect (15), together with our panel of HER2^{lo} and HER2^{hi} cells, and the MDA-MB-231 mesenchymal TNBC line. We quantified the bystander effect by comparing the response to T-DXd of various cells with low expression of HER2 in monoculture

versus co-culture with HER2^{hi} cells. While we confirmed the previously reported bystander effect with the MDA-MB-468 TNBC cell line, we observed minimal bystander activity in the other cell line co-cultures (**Fig. 3B**). We then investigated if the difference between MDA-MB-468 cells and the other HER2 low lines was due to their sensitivity to the DXd payload alone, finding that MDA-MB-468 cells were significantly more sensitive to DXd than the other cell lines (**Fig. 3C**). These results indicate that the T-DXd bystander effect is determined by the inherent sensitivity of the target cells to DXd.

To investigate the influence of co-culture on the clonal dynamics of HER2^{hi} and HER2^{lo} cells, we employed a DNA barcoding strategy and uniquely labelled cells in each population using the ClonMapper library (23). We compared clonal selection of HER2^{hi} and HER2^{lo} populations in the HCC1954 and 21PT models grown either in monoculture or in a 1:1 co-culture, under treatment with DMSO, neratinib or T-DXd for up to 10 passages (**Fig. 3D**). The ratio of HER2^{hi} to HER2^{lo} cells and the time per passage were monitored throughout the experiment and we again observed that treatment with T-DXd led to a rapid outgrowth of HER2^{lo} cells, but not treatment with neratinib, in HCC1954 cells (**Fig. 3E, Supplementary Fig. S5A**). In this model, HER2^{lo} completely outcompeted HER2^{hi} cells within just four passages, marking the endpoint of this treatment condition (**Fig. 3E**). Barcode sequencing revealed a decrease in clonal diversity over time across all groups, as evidenced by a decrease in Shannon entropy and a reduction in the number of most frequent barcodes needed to cover 90% of the final population (**Fig. 3F** and **3G, Supplementary Fig. S5B, S5C** and **S5D**). Both changes were more pronounced in the presence of HER2-targeting agents compared to DMSO, indicating selection for treatment-resistant subclones. Additionally, for cells treated with T-DXd, we observed significant differences when comparing co-culture to monoculture conditions. In HER2^{hi} cells treated with T-DXd, the reduction in clonal diversity was less pronounced in co-culture conditions, indicating reduced selection (**Fig. 3F** and **3G, Supplementary Fig. 5B, S5C,** and **S5D**). In contrast, HER2^{lo} cells experienced stronger selection when co-cultured with HER2^{hi} cells, suggesting the presence of a bystander effect.

Assessing the identity of the top 30 most abundant barcodes revealed that different clones were selected by neratinib and T-DXd treatment indicating different mechanisms of resistance (**Fig. 3H, Supplementary Fig. S5E** and **S6A**). The high similarity in clonal selection patterns between replicates and across monoculture and co-culture conditions in most conditions suggests that resistance is largely driven by pre-existing cellular traits. One exception to this pattern were HCC1954 $HER2^{hi}$ cells under T-DXd treatment which exhibited greater variability in barcode selection across replicates. While shared barcodes were also observed between those replicates, this greater variability suggests that stochastic or acquired mechanisms may also contribute to resistance in this condition. Further, we assessed differential selection of barcodes between conditions by testing for differences in the relative frequencies of the top 30 barcodes and correcting for multiple hypothesis testing (Methods). We found significant differential selection between monoculture and co-culture in all conditions except for $HER2^{hi}$ cells treated with neratinib (**Supplementary Fig. S6B**).

Based on these data, we conclude that $HER2^{hi}$ and $HER2^{lo}$ cells influence each other's phenotype in co-culture, thereby impacting therapeutic responses.

The impact of HER2 heterogeneity on tumorigenesis and treatment outcomes in vivo

Subsequently, we performed xenograft assays to assess the impact of HER2 heterogeneity on tumor growth and response to HER2-targeted therapies in vivo. We injected $HER2^{hi}$ or $HER2^{lo}$ cells alone (homogeneous) or as a 1:1 mix (heterogeneous) into the mammary fat pad of immunodeficient NSG mice. We found that $HER2^{lo}$ cells were unable to form tumors on their own, but both $HER2^{hi}$ homogeneous and heterogeneous tumors grew well in all three models tested (**Fig. 4A** and **Supplementary Fig. S7A**). We verified the presence of $HER2^{lo}$ H2B-GFP+ and $HER2^{hi}$ H2B-mCherry+ cells within tumors by fluorescence imaging and confirmed by immunofluorescence for HER2 that they retained their low and high levels of HER2 expression, respectively (**Fig. 4B** and **Supplementary Fig. S7B**). Intriguingly, $HER2^{lo}$ cells were maintained in

heterogeneous tumors despite their lack of tumor-initiating capacity. Investigating the spatial distribution of the cells within the tumors, we observed that $HER2^{hi}$ and $HER2^{lo}$ cells grew in clusters, with $HER2^{hi}$ cells more frequently neighboring other $HER2^{hi}$ cells, and similarly, $HER2^{lo}$ cells being more commonly surrounded by $HER2^{lo}$ cells (**Fig. 4B** and **4C**). We detected the same pattern in human HER2-positive tumors based on spatial analysis using CycIF in the NCT02326974 clinical trial cohort (20) (**Fig. 4D**).

To better understand the cell population dynamics during tumor growth, we performed a time-course experiment, monitoring the ratios of $HER2^{hi}$ and $HER2^{lo}$ cells in the tumors by flow cytometry (**Supplementary Fig. S7C and S7D**). $HER2^{lo}$ cells initially make up a substantial proportion of the tumors, but their ratio decreases during the exponential growth phase as the $HER2^{hi}$ population increases. This observation suggests that $HER2^{lo}$ cells can persist after injection but are less proliferative than $HER2^{hi}$ cells. Quantitative assessment of cellular proliferation by immunofluorescence for the S-phase marker PCNA demonstrated that PCNA+ cells were significantly more commonly $HER2^{hi}$ than $HER2^{lo}$, which was also observed in the CycIF data of the human cohort (20) (**Fig. 4E, 4F,** and **4G**).

To study the interaction of the $HER2^{hi}$ and $HER2^{lo}$ cells with their environment, we focused on human tumors. We performed scRNA-seq of our two HER2 heterogeneous tumors (T537, T565) (**Fig.4H** and **4I**) and analyzed these data with CellChat, which revealed that tumor cells with low levels of HER2 had greater amount of interaction with stromal cells than $HER2^{hi}$ tumor cells (**Fig.4J**). Dominating the signal affecting $HER2^{lo}$ cells were extracellular matrix (ECM) proteins like collagen and laminin (**Fig. 4K**). This observation was also consistent with analyses of a publicly available data set of six HER2+ breast tumors (24), which also showed collagen as the most enriched signal in $HER2^{lo}$ cells (**Supplementary Fig. S7E, S7F,** and **S7G**). Furthermore, we investigated whether $HER2^{lo}$ cells are in close proximity to different stromal cells with the CycIF data set (20), and we observed that their neighborhood are enriched in Podoplanin+ stromal cells (**Fig. 4L** and **Supplemental S7H**).

We next sought to evaluate the response of HER2 homogeneous and heterogeneous tumors to HER2-targeting therapies. To this end, mice with palpable tumors were randomly assigned to vehicle, neratinib (40 mg/kg), or T-DXd (10 mg/kg) treatment groups and treated for two weeks (**Fig. 4M**). Both neratinib and T-DXd treatment reduced the size of both HER2 homogeneous and heterogeneous tumors (**Fig. 4N** and **4O,** and **Supplementary Fig. S7I**). However, T-DXd was significantly more effective in $HER2^{hi}$ homogeneous compared to heterogeneous tumors, leading to complete regression in all cases, while the efficacy of neratinib was not affected by HER2 heterogeneity. Residual HER2 heterogeneous tumors following T-DXd treatment were predominantly composed of H2B-GFP+ $HER2^{lo}$ cells based on green fluorescence of the tumors, which we confirmed by immunofluorescence and flow cytometry (**Fig. 4O** and **4P**). In contrast, this shift in $HER2^{hi}$ and $HER2^{lo}$ cell populations was not observed in tumors from neratinib-treated mice. To better reflect the clinical setting, we also administered 8 continuous rounds of T-DXd (1 mg/kg every week) (Supplementary Fig. S7J). This regimen also led to a greater response in homogeneous tumors than heterogeneous tumors (**Supplementary Fig. S7K** and **S7L**).

To assess the impact of these treatments on recurrence and long-term survival, we followed mice bearing HER2 homogeneous or heterogeneous tumors after stopping T-DXd and neratinib treatment (**Fig. 4Q**). We observed that neratinib treated tumors recurred quickly after stopping treatment and that there was no difference in time to recurrence between HER2 homogeneous and heterogeneous tumors (**Fig. 4R** and **4S**). In contrast, tumors in T-DXd treated mice took more time to regrow with HER2 heterogeneous tumors recurring earlier than homogeneous ones (**Fig. 4R** and **4S**). A subset of mice (2 out of 5) with HER2 homogeneous tumors did not have recurrence more than 140 days after stopping T-DXd treatment, whereas all heterogeneous tumors recurred within 92 days (**Fig. 4R and 4S**). Moreover, recurrent HER2 heterogeneous tumors were predominantly composed of $HER2^{hi}$ cells in contrast to the tumors collected at the end of short-term T-DXd treatment (**Fig. 4T**). These $HER2^{hi}$ cells regained HER2 expression and were still

amplified at the *ERBB2* locus (**Supplementary Fig. S7M** and **S7N**). This observation recapitulates the experience in the NCT02326974 clinical trial, where non-heterogeneous residual tumors after T-DM1 and pertuzumab treatment had a decreased HER2 immunohistochemistry score, but did not have changes in their *ERBB2* FISH status (16). Therefore, when we culture the cells from the recurrent tumors, we observed that they are still sensitive to T-DXd (**Supplementary Fig. S7O**). Thus, while rare $HER2^{hi}$ cells may resist T-DXd and recover after treatment, these findings suggest that in heterogeneous tumors, $HER2^{lo}$ cells resistant to T-DXd may help sustain the fitness of some $HER2^{hi}$ cells, as they might then have a greater capacity to recover after discontinuation of treatment.

Overall, our xenograft experiments confirm that the presence of $HER2^{lo}$ cells drives therapeutic resistance to T-DXd in HER2 heterogeneous tumors.

Identification of sensitizers to T-DXd

Based on our data, increasing the efficacy of T-DXd in HER2 heterogeneous tumors would require the targeting of $HER2^{lo}$ cells either by drugs that specifically inhibit them or by enhancing their sensitivity T-DXd via synthetic lethal interactions. To identify such targets, we performed a whole-genome CRISPR-Cas9 knock out (KO) viability screen in $HER2^{lo}$ cells in co-culture with $HER2^{hi}$ cells treated with vehicle control or T-DXd for one month (**Fig. 5A**). We identified sgRNAs preferentially depleted (synthetic lethal hits) or enriched (resistance hits) in the presence of T-DXd but not in vehicle control using the maximum-likelihood analysis of gene essentialities (mle) from the MAGeCK pipeline (25) (**Supplementary Table S7**). GSEA analysis of the hits revealed resistance associated with mTOR signaling, basal transcription factors, and cellular senescence, while synthetic lethality involved aminoacyl-tRNA biosynthesis, nucleotide excision repair, and ubiquitin-mediated proteolysis (**Fig. 5B**).

Because our goal was to improve sensitivity to T-DXd, we prioritized the synthetic lethal hits and selected two of the top hits with preferential drop out in the T-DXd treated group, *ABCC1* (ATP

binding cassette subfamily C member 1) transporter and *USP9X* (Ubiquitin Specific Peptidase 9 X-linked), which have available pharmacological inhibitors (**Fig. 5C**). Furthermore, *USP9X* was selected because it offered the potential for a novel vulnerability, as it was not directly linked to established DXd efficacy pathways like other hits including *PRKDC* (DNA repair) and *BCL2L1* (apoptosis). We first generated derivates of $HER2^{lo}$ cells in the 21NT and HCC1954 models with two individual sgRNAs for both genes to validate the CRISPR screen results (**Supplementary Fig. S8A**). Next, we tested the sensitivity of these KO cells to T-DXd together with pharmacologic inhibitors of ABCC1 (reversan and biricodar) and USP9X (G9 and FT709) and confirmed that the inhibition of ABCC1 or USP9X sensitizes cells to T-DXd (**Fig. 5D** and **Supplementary Fig. S8B**). The expression of ABCC1 was increased in HCC1954 TDR cells (**Supplementary Fig. S8C**) and pharmacologic inhibition of both ABCC1 and USP9X enhanced the growth inhibitory effects of T-DXd in TDR resistant lines (**Fig. 5E** and **Supplementary Fig. S8D**). ABCC1 (also known as Multidrug resistance-associated protein 1, MRP1), promotes therapeutic resistance by transporting multiple compounds, including chemotherapeutic agents, out of the cells (26,27). Hence, we tested whether its inhibition sensitizes the cells to T-DXd by increasing the efficacy of its payload, DXd. We found that both genetic and pharmacologic inhibition of ABCC1 potentiated the growth suppressing effect of DXd while loss of USP9X activity had no effect (**Fig. 5F** and **Supplementary Fig. S8E**). Because the bystander effect of T-DXd is defined by the sensitivity of the neighboring cells to DXd, we also observed that ABCC1 inhibition increased the bystander effect of T-DXd in $HER2^{hi}$ and $HER2^{lo}$ cell co-cultures (**Fig. 5G** and **Supplementary Fig. S8F**). Notably, *ABCC1* expression was the lowest in the cell line most sensitive to DXd, MDA-MB-468, compared to the others (**Fig. 3C** and **Supplementary Fig. S8G**).

We then tested the effect of combining the ABCC1 inhibitor reversan with T-DXd on tumor growth and recurrence-free survival of mice with HER2 heterogeneous tumors (**Fig. 5H**). Reversan alone had no impact on tumor growth and the recurrence rate after discontinuing treatment (**Fig. 5I** and **5J**). However, its combination with T-DXd led to more pronounced suppression of tumor

growth and prolonged recurrence-free survival (**Fig. 5I** and **5J**). Flow cytometry analysis of the cellular composition of recurrent tumors showed no significant changes in the relative fraction of $HER2^{hi}$ and $HER2^{lo}$ cells (**Supplementary Fig. S8H**), although there were few $HER2^{lo}$ cells, thus, the potentiation of the bystander effects of T-DXd cannot be excluded. Therefore, inhibiting ABCC1 presents a promising therapeutic strategy to enhance the efficacy of T-DXd, which is interesting in a HER2 heterogeneous context that can benefit from an increased bystander effect.

To gain mechanistic insight into the mechanism by which USP9X sensitized $HER2^{lo}$ cells T-DXd, we first evaluated if inhibition of USP9X also increases the efficacy of other HER2-targeting ADCs like T-DM1. We found that both genetic deletion and pharmacologic inhibition of USP9X sensitized both $HER2^{lo}$ cells and TMR cells to T-DM1 (**Supplementary Fig. S9A**), suggesting that its mechanism of action is not specific to T-DXd. Thus, we explored how USP9X inhibition affected EGFR/HER2 signaling by immunoblot analysis for components of the signaling pathway, but we did not observe any significant effects (**Supplementary Fig. S9B**). USP9X inhibition also did not change the cell surface levels of HER2 at baseline or after T-DXd treatment as assessed by flow cytometry in $HER2^{lo}$ cells (**Supplementary Fig. S9C** and **S9D**). However, we detected a pronounced increase of ubiquitinated HER2 in the presence of T-DXd upon USP9X inhibition (**Fig. 6A** and **Supplementary Fig. S9E**). To test if USP9X directly interacts with HER2, we immunoprecipitated HER2 or USP9X from both $HER2^{hi}$ and $HER2^{lo}$ cells and performed immunoblot assays for both proteins. HER2 was detected in USP9X immunoprecipitates, and conversely, USP9X was present in HER2 immunoprecipitates (**Fig. 6B** and **Supplementary Fig. S9F**). We also performed proximity ligation assay (PLA) experiments that confirmed an interaction between HER2 and USP9X in both $HER2^{hi}$ and $HER2^{lo}$ cells (**Fig. 6C** and **Supplementary Fig. S9G** and **S9H**), also showing that the interaction was further increased following T-DXd treatment. Subsequently, we investigated if USP9X deletion or inhibition leads to enhanced degradation of HER2 in the presence of T-DXd, finding that the reduction of HER2 protein levels following 48h of treatment with T-DXd was potentiated by USP9X inhibition in both $HER2^{lo}$ and $HER2^{hi}$ cells (**Fig.**

6D and **Supplementary Fig. S9I**). To assess HER2 protein stability in these treatment conditions, we performed cycloheximide pulse chase experiments. These analyses revealed a decrease in HER2 stability upon T-DXd treatment combined with USP9X inhibition (**Fig. 6E** and **6F**).

Since HER2 is internalized and transported to the lysosomes after T-DXd treatment, we next assessed if USP9X inhibition increases the fraction of HER2 in the lysosomes by performing PLA experiments between HER2 and LAMP1. We detected a significant increase of HER2 in the lysosomes after T-DXd treatment which was further potentiated with USP9X inhibition (**Fig. 6G** and **6H, Supplementary Fig. S9J** and **9K**). This finding was also validated by immunoblot for HER2 using lysosome-enriched cell fraction of $HER2^{lo}$ cells (**Fig. 6I** and **Supplementary Fig. S9L**). Therefore, we conclude that HER2 is more efficiently targeted to lysosomes upon T-DXd treatment when USP9X is inhibited, which is shown to lead to an increase of the ADC payload release and cell death (7).

To validate the clinical relevance of our findings, we investigated the expression of *USP9X* in our RNA-seq data comparing HER2+ tumors before and after T-DM1 + pertuzumab neoadjuvant treatment from the NCT02326974 clinical trial (9,16). We found that the expression of *USP9X* was higher in post- compared to pre-treatment tumors in patients who did not achieve a pCR, in both non-heterogeneous (no HET) or heterogeneous (HET) tumors (**Fig. 6J**), confirming that increased expression of *USP9X* is likely a clinically relevant mechanism of resistance to HER2-targeting ADCs.

Lastly, we tested the therapeutic potential of combining T-DXd and USP9X inhibitors for the treatment HER2 heterogeneous tumors (**Fig. 6K**). USP9X inhibition alone had no effect on tumor growth and recurrence-free survival (**Fig. 6L** and **6M**). However, its combination with T-DXd led to more pronounced tumor suppression and it significantly increased recurrence-free survival with a few mice remaining tumor-free in the time frame of the experiment (**Fig. 6L** and **6M**). USP9X inhibition did not affect the relative fraction of $HER2^{hi}$ and $HER2^{lo}$ cells in residual tumors, although

again there were very few HER2^{lo} cells detected, thus, differences in the effect of USP9X inhibition on cells with different HER2 levels cannot be excluded (**Supplementary Fig. S9M**).

Overall, our data show that targeting USP9X or ABCC1 can offer an effective therapeutic strategy to improve the efficacy of T-DXd in HER2 heterogeneous tumors (**Fig. 6N**).

DISCUSSION

Here we describe unique models of HER2-positive breast cancer that accurately recapitulate key aspects of clinical HER2 heterogeneous breast tumors. Specifically, $HER2^{hi}$ and $HER2^{low}$ cells in the three models we identified display differences in *ERBB2* amplification, PAM50 subtype, proliferation rates, *in vivo* growth patterns, and response to HER2-targeting therapies in line with observations in HER2 heterogeneous breast cancer in patients. Even if some limitations exist of using cell line models including reduced complexity and lack of microenvironmental components compared to human tumors, our characterization of these models and use for the discovery of new therapeutic targets underscores their potential utility for deepening our understanding of HER2 heterogeneous breast cancer and to develop more effective treatment strategies for patients with HER2 heterogeneous disease. This work also proposes HER2 heterogeneity as a biomarker for treatment decision, as they are more likely to be resistant to HER2-targeting ADCs.

The evolutionary paths of HER2 heterogeneous tumors and the origin of *ERBB2*-non-amplified cells in HER2-positive breast cancer are poorly understood. Our prior studies investigating cellular heterogeneity for *ERBB2* amplification and mutant *PIK3CA* in HER2-positive tumors using STAR-FISH suggested that *ERBB2* amplification precedes *PI3KCA* mutation implying that $HER2^{lo}$ cells might evolve from $HER2^{hi}$ cells due to downstream activation of the signaling pathway eliminating the selective advantage of HER2 gain (28). Our profiling of HER2 heterogeneous breast tumors in the NCT02326974 clinical trial (9) and $HER2^{hi}$ and $HER2^{lo}$ populations in our preclinical models support this hypothesis, since $HER2^{lo}$ cells had high activity of downstream signaling despite low levels of HER2. However, alternative models like the subclonal gain of *ERBB2* amplification at later stages of tumor evolution cannot be excluded.

The newer generation of HER2-targeting ADCs including T-DXd showed impressive results in HER2+ breast cancer and had remarkable efficacy even in patients with HER2-low tumors that would not respond to classic HER2-targeting agents like trastuzumab (29,30). According to results from the DESTINY-Breast09 trial, the combination of T-DXd and pertuzumab demonstrated a

clinically meaningful improvement over the current standard first-line therapy for metastatic HER2-positive breast cancer, suggesting it may be practice-changing (31). Therefore, elucidating the mechanisms of resistance to this regimen and identifying potential therapeutic vulnerabilities upon treatment failure are critical for optimizing patient outcomes.

An interesting property of T-DXd is that it has a cleavable linker and a cell permeable payload and hence has a bystander effect killing neighboring cells even if they do not express the target (15). Consequently, it has been hypothesized that T-DXd will be effective against HER2 heterogenous tumors compared to T-DM1, but so far there is no clinical data supporting this claim. Furthermore, a recent study showed a decrease of HER2 expression and T-DXd binding as a cause of resistance in human tumors (32) . Our models demonstrate that residual disease remained in HER2-heterogeneous tumors after T-DXd treatment, and although these tumors were primarily composed of $HER2^{lo}$ cells, the recurrent tumors were still mainly $HER2^{hi}$. Thus, $HER2^{lo}$ cells resistant to T-DXd can drive tumor recurrence by promoting the regrowth of $HER2^{hi}$ cells, confirming that HER2 heterogeneity drives resistance to T-DXd. Furthermore, our study demonstrates that the bystander effect of T-DXd is highly dependent on the intrinsic sensitivity of neighboring cells to DXd, as the concentration they receive may be insufficient for a cytotoxic response.

With our models, we show that $HER2^{lo}$ cells are sensitive to HER2 kinase inhibitors tucatinib and neratinib, suggesting that despite the lack of HER2 amplification, these cells are dependent on EGFR/HER2 signaling for survival. Therefore, by treating with a combination of both types of HER2-targeting agents, we could affect both $HER2^{lo}$ and $HER2^{hi}$ cells in heterogeneous tumors. Additionally, irreversible pan-HER inhibitors such as neratinib promote receptor ubiquitination, thereby enhancing ADC internalization and therapeutic efficacy (21,22,33). Therefore, in HER2-heterogeneous tumors, the combination of HER2 kinase inhibitors and ADCs inhibits HER2 activity across both cell populations, including ADC-resistant $HER2^{lo}$ cells, while also enhancing ADC efficacy. As this combination might be too toxic to apply as first line of treatment, we sought to

identify alternative options. Our findings based on the CRISPR screens suggest that enhancing T-DXd efficacy in HER2^{lo} cells may represent a promising strategy to improve outcomes in HER2-heterogeneous tumors. Two of the top hits, ABCC1 and USP9X, we further characterized are candidate targets to be applied in combination with HER2-targeting ADCs for the more effective treatment of HER2 heterogeneous breast tumors. ABCC1 is a multidrug resistance protein, a well-established mediator of drug resistance through its ability to promote the efflux of various therapeutic agents from cancer cells (27,34). Although inhibitors in ABC transporters have been tested in clinical trials in treatment-resistant cases, they failed to progress into clinical practice potentially due to suboptimal patient selection and the use of inhibitors with poor specificity and potency, which may have led to limited efficacy and increased toxicity (35). Our study provides a new perspective on the application of ABCC1 inhibitors as combination agents in early-stage disease to enhance drug efficacy upfront instead of trying to re-sensitize drug-resistant tumors.

Our discovery of USP9X, a deubiquitinating enzyme that we showed regulates HER2 protein stability, as a synthetic lethal hit with T-DXd highlights the importance of HER2 itself as the key determinant of response to HER2-targeting agents. USP9X has been implicated in cancer progression and drug resistance through its role in pathways such as EGFR endocytosis, TGF-β, YAP1, and Notch signaling (36-39). Notably, its inhibitor G9 has previously been shown to reduce the growth of TNBC tumors in preclinical models (39). Furthermore, USP9X is an important regulator of apoptosis and mitotic cell death, functions that could also be contributing to its effect on T-DXd response (40-42). While a previous study showed a potential mechanistic relationship between USP9X and HER2 in the context of proteasome inhibition (43), USP9X has not been linked to HER2 ADC response. Our study proposes that combining its inhibition with T-DXd could be a new approach for the treatment of HER2 heterogeneous tumors. More studies on this combination potentially increasing adverse effects in normal tissues will be needed, even if one of the main toxicity related to T-DXd, pneumonitis, has been shown to be target-independent (44).

USP9X inhibitors are in the early stages of clinical development, limiting the direct translation of this finding, but our data and others justify continued drug discovery efforts in this space.

In conclusion, we show the potential of combining T-DXd with compounds that can increase HER2 targeting to the lysosomes or the sensitivity of cells to its payload. This finding is particularly relevant in HER2 heterogeneous tumors, as resistant HER2^{lo} cells drive recurrence after T-DXd treatment and could also broaden the applicability of T-DXd in HER2-low breast cancers (45,46). Furthermore, our findings have broader relevance beyond breast cancer, as HER2 heterogeneity has also been observed in other cancers, such as gastric cancer and high-grade endometrial carcinomas (47,48).

METHODS

Ethics statement

All human and animal studies were conducted in compliance with the relevant ethical guidelines and approved by the appropriate ethics committees. Animal experiments were carried out in an AAALAC-accredited SPF rodent-only barrier facility at Dana-Farber Cancer Institute (DFCI) following protocol 11-023 approved by DFCI Animal Care and Use Committee (ACUC). Human breast cancer samples were collected using protocol 93-085 (Nancy Lin, PI) approved by the Dana-Farber Cancer Institute Institutional Review Board and written informed consent were obtained from the patients. Consent was obtained from all participants or waived for deceased patients. Samples were deidentified prior to transport to the laboratory.

Cell lines and culture conditions

Human breast cancer cells lines MDA-MB-231 (RRID:CVCL_0062), HCC1954 (RRID:CVCL_1259), BT-474 (RRID:CVCL_0179), ZR-75-30 (RRID:CVCL_1661), SK-BR-3 (RRID:CVCL_0033), MDA-MB-361 (RRID:CVCL_0620) and MDA-MB-453 (RRID:CVCL_0418) were purchased from ATCC and 21NT (RRID:CVCL_7933) and 21PT (RRID:CVCL_7934) cells were provided by Arthur Pardee, Dana-Farber Cancer Institute. Cells were cultured in conditions recommended by the supplier and routinely tested for mycoplasma and murine pathogens. 21NT and 21PT cells were cultured with DMEM/F12, 5% Horse Serum, 10 μg/mL insulin, 20 ng/mL EGF and 0.5 μg/mL hydrocortisone. All cell lines were supplemented with 50 U/mL penicillin.

Flow Cytometry and Cell Sorting (FACS)

The panel of HER2+ breast cancer cell lines and MDA-MB-231 were stained using anti-HER2 PE or isotype control PE for 20 min at room temperature. Flow cytometry was performed using LSRFortessa (BD Bioscience, RRID:SCR_018655), analysis was done with FlowJo (version 10,

582 RRID:SCR_008520). To generate stable HER2^{hi} and HER2^{lo} cell lines, HCC1954, 21NT and 21PT
583 expressing H2B-mCherry or H2B-GFP were stained with anti-HER2 APC and sorted for either high
584 or low HER2 expression levels using the BD FACS Aria II cell sorter (RRID:SCR_018934) as
585 depicted in Figure 1A. After sorting, the cells were grown and resorted for HER2 levels 4 other
586 times. The antibodies used are listed in **Supplementary Table S8**.

587 For quantification of the tumor composition by flow cytometry, tumors were homogenized
588 using micro pestles immediately after collection and digested for 1 hour with digestion media (2%
589 wt/vol collagenase IV, 2% wt/vol hyaluronidase, and 2% wt/vol bovine serum albumin in
590 DMEM/F12) at 37°C on a shaker. The solutions were filtered through a 500 μm mesh (Tetko, 03-
591 500-47), washed with PBS, and frozen in 10% dimethyl sulfoxide/fetal bovine serum at −80°C to
592 preserve before flow cytometry of all samples at once. For the acquisition, cells were thawed,
593 washed with PBS and passed through a 35 μm cell strainer tube (Falcon) and analyzed using an
594 LSRFortessa (BD Biosciences, RRID:SCR_018655). All flow cytometry experiments were
595 performed at the DFCI Flow Cytometry Core (RRID:SCR_009751). The gating strategies are
596 depicted in **Supplementary Fig. S7D**.
597

598 **Fluorescent in situ hybridization (FISH)**

599 Cells were resuspended in 75 mM KCl, incubated for 10-20 minutes at room temperature and
600 washed in fixative (3:1 methanol-to-acetic acid). The cells were then spread onto a slide, allowing
601 the fixative to evaporate. Slides were washed with water, incubated with proteinase K solution in
602 PBS at 37°C for 2 minutes, followed by post-fixation in ice-cold Carnoy's solution (3:1 ethanol-to-
603 acetic acid). The slides were then subjected to ethanol washes and air-dried. Probe mix from
604 PathVysion HER2 DNA Probe Kit (Abbott) was applied to the slides, covered with a coverslip, and
605 sealed with rubber cement. The slides were incubated at 75°C for 7 minutes and then at 37°C
606 overnight in a humidified chamber. After hybridization, coverslips and rubber cement were

removed, and slides were placed in a 0.4x SSC/0.3% NP-40 wash solution at room temperature for 2 minutes, followed by incubation for 2 minutes in preheated at 74°C 0.4x SSC/0.3% NP-40 wash solution. Next, slides were washed 2 times for 2 minutes in SSC/0.1% NP-40 at room temperature, followed by a 3-minute wash in 2x SSC at room temperature. Slides were then mounted using DAPI mounting medium (Vector Laboratories) and imaged using Nikon ECLIPSE Ti2-E fluorescence microscope for quantification and confocal Zeiss 980 (RRID:SCR_025048) from the Molecular Cancer Imaging Facility in Dana-Farber Cancer Institute for figure image.

Immunoblot analyses

Cells were lysed with RIPA lysis buffer (50 mM Tris pH 7.6, 0.1% SDS, 1% NP-40, 150 mM NaCl, 5 nM EDTA), supplemented with phosphatase and protease inhibitors (Fisher Scientific). Protein concentration was determined using the Pierce™ 660 nm Protein Assay Reagent (Thermo Fisher), and proteins were heat-denatured in the presence of β-mercaptoethanol. Equal amounts of protein were loaded onto a NuPAGE Novex 8% or 4–12% gradient Bis-Tris gel (Fisher Scientific) and separated by electrophoresis. Proteins were transferred to PVDF membranes (Bio-Rad) using a wet NuPAGE transfer system, with transfer buffer containing 20% methanol, for 1 hour 30 minutes at 90 V. The membranes were then blocked with blocking buffer (5% BSA in 0.1% Tween20 TBS (TBST)) for 1 hour at room temperature, followed by overnight incubation with primary antibodies in blocking buffer. Membranes were washed and incubated for 30 minutes at room temperature with the appropriate secondary antibodies. The antibodies used are listed in **Supplementary Table S8**. After additional washing, the membranes were developed using Clarity™ Western ECL substrate (Bio-Rad) and imaged with the ChemiDoc MP imaging system (Bio-Rad, RRID:SCR_019037). Quantification of immunoblots were performed using the Gels function of FIJI (RRID:SCR_002285).

Short tandem repeat (STR) and Whole Exome Sequencing (WES)

DNA isolation from cells was performed using DNeasy Blood & Tissue Kit (Qiagen). gDNA was fragmented to 200bp on a Covaris R230 instrument according to manufacturer's protocol. Libraries were prepared using IDT xGEN 2S Plus DNA reagents on a Beckman Coulter Biomek i7 liquid handling platform from approximately 200 ng of DNA according to manufacturer's protocol with 14 cycles of PCR amplification. Finished libraries were quantified by Qubit fluorometer and fragment size distribution was evaluated by Agilent TapeStation 4200 (RRID:SCR_019547). Libraries were pooled together for target enrichment using Twist Exome v2.0 reagents and hybrid capture was performed with a 16-hour hybridization incubation using a custom probe panel according to manufacturer's protocol. Post-capture library pools were quantified by Qubit fluorometer and Agilent TapeStation 4200 (RRID:SCR_019547). Library pools were further evaluated for quality and pool balance with shallow sequencing on an Illumina MiSeq (RRID:SCR_016379). Subsequently, libraries were sequenced on an Illumina NovaSeqX+ with paired-end 150 bp reads by the Molecular Biology Core Facilities at Dana-Farber Cancer Institute (RRID:SCR_009754).

Sequenced reads (FASTQ files) were aligned to hg38 version of human genome with BWA-MEM v.0.7.15 (RRID:SCR_022192) and preprocessed following GATK (RRID:SCR_001876) best practices (14). The quality of alignment and potential sample contamination was evaluated with the following software tools FastQC (RRID:SCR_014583), Picard (RRID:SCR_006525), and FastQ-Screen (RRID:SCR_000141). Short nucleotide variants (point mutations and indels) were called using GATK Mutect2 (RRID:SCR_001876) using a "panel of normals" based on samples from the 1000 Genomes Project (RRID:SCR_008801) and provided in the Broad Institute's public data repository. Identified variants were annotated with VEP (49) and transformed into MAF files with the vcf2maf script. The variant calls were further annotated with OncoKB (RRID:SCR_014782) using the oncokb-annotator python package. Copy number segment files were produced by CNVkit (RRID:SCR_021917) (50) utilizing a 'flat' genome reference file to reduce background noise. The list of the most mutated genes from patients' samples was generated using cBioPortal platform (https://www.cbioportal.org/, RRID:SCR_014555) selecting for breast cancer patients in

TCGA cohort. Finally, the STR profiling was performed by the Dana-Farber Cancer Institute Molecular Diagnostics Labs Research Services.

CyTOF

Antibodies used for CyTOF were obtained in carrier-free solutions and conjugated to lanthanide metals by the CyTOF Antibody Resource and Core Facility at Brigham and Women's Hospital. Cells were cultured in 10 cm dish and gently detached using detach cells with Cell dissociation buffer (Gibson) to preserve surface proteins. Approximately 1 × 10^6 cells per condition were incubated with 100 μmol/L Rhodium intercalator (^103Rh; Fluidigm) for 30 minutes at 37°C in complete media. Samples were then barcoded using the Cell-ID 20-Plex Pd Barcoding Kit (Fluidigm) per manufacturer's instructions and barcoded samples were pooled and processed together.

Cells were fixed with 1.6% paraformaldehyde (Electron Microscopy Sciences) for 10 minutes, blocked with Human TruStain FcX (BioLegend) for 10 minutes, and stained with surface antibodies for 30 minutes at room temperature. Following surface staining, cells were permeabilized in methanol on ice for 10 minutes and incubated with intracellular antibody cocktail for 30 minutes. Cells were then fixed overnight at 4°C in Fix and Perm Buffer (Fluidigm) containing 62.5 nmol/L Intercalator-IR (Fluidigm). Prior to acquisition, samples were washed in Cell Acquisition Solution (CAS; Fluidigm), resuspended in CAS with EQ Four Element Calibration Beads (1:10 dilution; Fluidigm), and filtered through a 35 μm strainer. Data were acquired on a Helios CyTOF mass cytometer (Fluidigm, RRID:SCR_019916), normalized as previously described, and analyzed using Cytobank (RRID:SCR_014043). All staining steps and washes were performed using Cell Staining Media (PBS with 0.5% BSA and 0.02% sodium azide). For analysis, cells were gated for intact singlets, viable (Rh^103-negative), and non-apoptotic (cleaved PARP-negative) populations. viSNE clustering was performed on the c-PARP-negative population. The antibodies used are listed in **Supplementary Table S8**.

RNA-seq

RNA was isolated using the RNeasy Mini Kit (QIAGEN) and libraries were prepared using the KAPA mRNA HyperPrep (Roche) strand-specific sample preparation kits from 100 ng of purified total RNA, following the manufacturer's protocol on a Biomek i7 (Beckman Coulter). The resulting double-stranded DNA libraries were quantified using a Qubit fluorometer (Thermo Fisher Scientific) and the 4200 TapeStation (Agilent, RRID:SCR_018435). The final library pool was sequenced on an Illumina NovaSeq 6000 (Illumina, RRID:SCR_016387), targeting 40 million 150-bp read pairs per library at the Dana-Farber Cancer Institute Molecular Biology Core Facilitiy (RRID:SCR_009754). RNA-seq data were processed using the VIPER pipeline (51). Fastq files were aligned to the human reference GRCh37/hg19 genome with the STAR RNA-Seq aligner (version STAR_2.5.1b, RRID:SCR_004463) (52), followed by transcript assembly with Cufflinks v2.2.1 (RRID:SCR_014597) and RSeQC v2.6.2 (RRID:SCR_005275) (53). Differential gene expression analyses were conducted on absolute gene counts for RNA-Seq data and raw read counts for transcriptomic profiling data using DESeq2 v1.18.1 (RRID:SCR_000154) (54). Gene set enrichment analysis (GSEA, RRID:SCR_003199) was performed using the Broad GSEA Application (GSEA Java; v4.1.0) with Hallmark gene sets v7.4 (55,56). PAM50 subtype prediction was carried out using the genefu package, and the resulting subtype probabilities were used to estimate the likelihood of each molecular subtype for each sample.

CycIF and spatial analysis

For the heterogeneous tumor images, cells were annotated according to the nuclei staining of mCherry ($HER2^{hi}$), GFP ($HER2^{lo}$) or only positive for Dapi (Other). Cell nuclei images were segmented and labeled using cellpose 4.0.4 pretrained model with flow threshold set to 0.4 and cellprob threshold to 0. Centroid were computed using scikit-image 0.24.0. For the CycIF cohort, data annotations and coordinates from the original paper were used (20). For both sets, spatial

analysis was performed using scimap 2.3.4 in python 3.9 (RRID:SCR_008394). Preprocessing of the data sets was done with using pandas 2.2.3. Preprocessing involved filtering irrelevant data, removing scenes that contained too few cells of interest. Spatial analysis was accomplished using scimap spatial count function with the KNN method, K=11. The method determines the 10 nearest neighbors for each cell, irrespectively of physical distances. Composition of neighborhoods is then averaged out for each cell type.

Treatment, dose response and growth assay

1000 cells were plated in 96-well plates (6 days experiments) or in 48-well plates (9-12 days growth assays). Trastuzumab deruxtecan (T-DXd, MedChemExpres HY-138298) and trastuzumab emtansine (T-DM1, MedChemExpress HY-P9921) were in dissolved PBS. Neratinib (MedChemExpress HKI-272), irbinitinib (tucatinib, Selleckchem S8362), deruxtecan (DXd, MedChemExpress HY-13631E), paclitaxel (Sigma T7191), G9 (EOAI3402143, MedChemExpress HY-111408), FT709 (MedChemExpress HY-145967), reversan (Selleckchem E1742) and biricodar (Selleckchem E1781) were dissolved in dimethyl sulfoxide. G9, FT709, reversan and biricodar were used at a concentration of 1 μM. Plates were imaged with Celigo Image Cytometer (Nexcelom Bioscience, RRID:SCR_018808) to count cells based on the nuclear H2B-mCherry or H2B-GFP signal from the cells, or Hoechst 33342 (Life Technologies) staining. For pulse-chase experiments, cycloheximide (Sigma, 100 μg/mL) was added in 6 well plates for the indicated times.

Patient derived organoids (PDOs)

Primary tumors collected fresh from Brigham and Women's Hospital and the patient-derived PDX were dissociated using 2 mg/mL BSA, 2 mg/mL collagenase type IV (Worthington Biochemical Corporation, Cat# LS004189), 2 mg/mL hyaluronidase (Sigma-Aldrich, Cat# H3506) in DMEM/F12 media, filtered through a 500 μm strainer and frozen viable in FBS 10% DMSO. T537 is a grade 3, HER2+ IDC, ER low-positive, untreated. T565 is ER+, PR+ and HER2+ IDC. The patient-derived

xenograft Mets15 is derived from ascites of a tumor classified as ER+, PR+, HER2- treated with chemo, AI and fulvestrant, but shows positive heterogeneous IHC staining for HER2, also confirmed by flow cytometry during this experiment (57). After recovery, organoids were generated as described (58). Brefly, cells were resuspended in Matrigel and 50 µL droplets where place into 24-well plate. 700 µL of organoid culture medium (advanced DMEM/F12 supplemented with 1% GlutaMax (Gibco, Cat# 35050061), 1% HEPES (1 M), 1% penicillin/streptomycin, 0.1% amphotericin B (Gibco, CAS# 1397-89-3), 1X B27 supplement (Gibco, Cat# 17504044), 500 ng/mL recombinant R-spondin (Peprotech, Cat# 120-38), 1.25 mM N-acetylcystine (Sigma-Aldrich, CAS# 616-91-1), 10 mM Nicotinamide (Sigma-Aldrich, CAS# 98-92-0), 1 µM SB202190 (Sigma-Aldrich, CAS# 152121-30-7), 5 ng/mL FGF7 (Peprotech, Cat# 100-19), 20 ng/mL FGF10 (Peprotech, Cat# 100-26), 5 nM heregulin beta-1 (Peprotech, Cat# 100-03), 5 ng/mL EGF (Peprotech, Cat# AF-100-15)) was added to cover the matrix. Subsequently, the medium was changed every 3 days. For flow cytometry, organoids were dissociated in single cell suspensions using TrypLE Express Enzyme (Gibco) and HER2 staining was performed as described previously. For Mets15, RPF+ cancer cells were gated to eliminate normal murine cells from the analysis.

scRNA-seq library preparation

Tumor samples were digested as described in the PDOs section. To remove debris and non-viable cells, a Percoll density gradient (50%/40%/20% layers) was utilized. After a 30-minute centrifugation at 2000xg at 4°C without brakes, cells were recovered from the 20/40% interface. The cells were washed, filtered 100 µm, and resuspended in PBS + 0.04% BSA. Around 20,000 cells were processed using the 10x Genomics ChromiumTM instrument (10x Genomics) according to the manufacturer's recommendations and the library were generated using Chromium Next GEM Single Cell 5' HT Kit v2 (10x Genomics). Library quality was verified using Bioanalyzer High Sensitivity DNA Kit (Agilent). Sequencing was performed at the Dana-Farber Molecular Biology Core (RRID:SCR_009754) on an Illumina NovaSeq 6000 platform, generating 150bp paired-end

reads at a density of 40 million reads per library. EMBO cohort data were downloaded from Pal et al.(24), including only HER2+ and treatment naive tumors.

scRNA-seq data analysis

Copy number variation analysis

Copy number variations (CNVs) were inferred from single-cell RNA sequencing data using the inferCNV R package v 1.24.0 (RRID:SCR_021140). Tumor cells were defined based on the expression of epithelial markers, including EPCAM and keratins (KRT), and were selected from the integrated single-cell dataset. Immune and stromal cell populations, identified by the expression of lineage-specific markers such as PTPRC and COL1A1, were used as reference (normal) cells for CNV inference. Raw gene expression counts were used as input, and genes were ordered according to their chromosomal positions based on the human genome annotation. InferCNV was run with a cutoff value of 0.1, appropriate for 10x Genomics droplet-based scRNA-seq data. Expression values were normalized relative to the reference cell populations to estimate large-scale chromosomal copy number alterations in tumor cells. To reduce noise and identify coherent CNV patterns, inferCNV applied smoothing across adjacent genes along each chromosome, followed by unsupervised hierarchical clustering of tumor cells based on their inferred CNV profiles. In addition, a Hidden Markov Model (HMM) was used to segment the genome and classify chromosomal regions into discrete CNV states, including losses, neutral regions, and gains. CNV-defined tumor subclones were subsequently identified and used for downstream analyses and visualization.

CellChat

Processed count matrices from each cohort were first merged using Seurat (RRID:SCR_007322) (59). Low-quality cells were filtered using the following criteria: nCount_RNA > 1,000, nFeature_RNA < 1,000, mitochondrial gene percentage < 20%, ribosomal gene percentage < 40%, and log10(genes per UMI) > 0.8. Data normalization was performed using SCTransform

(RRID:SCR_022146), regressing out ribosomal percentage, mitochondrial percentage, nCount_RNA, and nFeature_RNA. Dimensionality reduction and clustering were performed using the top 30 principal components. Cell clusters were manually annotated using gene module scores based on curated marker gene sets. UMAP visualization was generated using the scCustomize package (RRID:SCR_024675). Cell-cell communication analysis was performed using CellChat (RRID:SCR_021946) (60) to infer ligand-receptor interactions between cell types. Overall information flow for each signaling pathway was extracted from the CellChat object, and differential pathway activity was assessed between $HER2^{hi}$ and $HER2^{lo}$ epithelial cells.

Generation of resistant cell lines

HCC1954, 21NT, and 21PT cells were culture for over 3 months in total starting with DMSO (Ctl) or doses close to IC50 (tucatinib 1 μM; neratinib 100 nM; T-DM1 10 ng/mL for HCC1954 and 100 ng/mL for 21NT and 21PT; T-DXd 100 ng/mL for HCC1954 and 1 μg/mL for 21NT and 21PT) and then increased after 2-3 passages when cells were growing (tucatinib 3 μM; neratinib 300 nM; T-DM1 30 ng/mL for HCC1954 and 300 ng/mL for 21NT and 21PT; T-DXd 300 ng/mL for HCC1954 and 3 μg/mL for 21NT and 21PT). For maintenance, cells were kept in their initial doses close to IC50.

Cell Barcoding and sequencing preparation

The high-complexity Clonmapper library (23) was a gift from Amy Brock. 5e5 cells were infected at a multiplicity of infection (MOI) of 0.1, corresponding to 10% BFP+ cells, to ensure integration of only one barcode per cell. BFP+ sorted cells were minimally expanded to allow the growth of enough cells to start the experiment. 5e5 cells were plated at the start of the experiments and the same amount was kept at each passage. Cells were then cultured for up to 10 passages in DMSO, neratinib (200 nM for HCC1954, 100 nM for 21PT) or T-DXd (50 ng/mL for HCC1954, 1 ug/mL for

21PT). HCC1954 T-DXd treated cells were stopped at 4 passages since HER2^{lo} cells already took over the co-culture condition. Cells from every passage were collected, and for the selected ones, genomic DNA was extracted using phenol/chloroform/isoamyl alcohol, and library preparation PCR was performed on the genomic DNA. The PCR conditions were changed from the previous publication, improving its reliability. We added a PCR step where the barcoding construct is amplified first with smaller primers (actcggtgccacttttttcaagttg and gagggcctatttcccatgattccttc). Then a second PCR was performed on the first reaction to add the adapters and barcodes for sequencing as in the original protocol (23).

Barcoding Analysis

Constant flanking sequences were trimmed from 151 base pair barcode sequencing reads using cutadapt version 4.2 (RRID:SCR_011841) (61). The cutadapt output was then filtered using seqtk version 1.3 (RRID:SCR_018927) to only retain reads of 20 base pairs, consistent with the length of the barcode sequence. Additionally, we filtered out barcodes that only had one read across all samples. Barcodes were categorized as belonging to the HER2^{hi} group if their relative frequency averaged over the pre-treatment HER2^{hi} monoculture samples was larger than their relative frequency averaged over the pre-treatment HER2^{lo} monoculture samples, and vice-versa for the HER2^{lo} group. Plots pertaining to the barcode data were generated in R version 4.4.1, using the packages ggplot2 (RRID:SCR_014601) and fishplot (62).

Diversity was quantified in two ways. Firstly, we calculated the minimum number of unique barcodes to jointly constitute at least 90% of the sample. Secondly, we calculated the Shannon Entropy,

$$Shannon\ Entropy = -\sum_i p_i \ln(p_i)$$

, where p_i denotes the relative frequency of the i-th barcode. For co-culture samples we calculated relative frequencies and the corresponding Shannon Entropy within the HER2^{hi} group and the HER2^{lo} group separately.

Testing for differential barcode selection across conditions. We apply a centered log ratio transform to the barcode frequencies of the top 30 barcodes. For each pair of conditions, we go over these top 30 barcodes and perform Welch's t-tests comparing the mean prevalence of a given barcode between the two conditions. We then rank all p-values per pairwise comparison, apply a Bonferroni correction, and report the smallest p-value. P-values below our significance threshold of 5% thus indicate that at least one barcode within the top 30 barcodes was differentially selected between conditions.

Reverse Phase Protein Array (RPPA)

HER2^{hi} and HER2^{lo} cells were place in mono or co-culture (1:1) for 8 days before collecting and sending cells to the Functional Proteomics RPPA Core Facility at MDAnderson Cancer Center (RRID:SCR_016649). Details of the RPPA platform as performed by the RPPA Core are described in (63). In brief, proteins were denatured using SDS and 2-mercaptoethanol and diluted lysates were arrayed on nitrocellulose-coated slides (Grace Bio-Labs) by the Quanterix 2470 Arrayer (RRID:SCR_027241). Slides were processed using validated primary antibodies and biotin-conjugated secondary antibodies. The signal was amplified via the GenPoint platform (Agilent Technologies) and visualized through DAB colorimetric staining. Following imaging with a TissueScope (Huron Digital Pathology), spot intensities were quantified using customized Array-Pro Analyzer software (Media Cybernetics). To determine relative protein levels, RPPA SPACE pipeline (64) was used. This method fits a logistic model to a single curve generated from all slide samples, treating signal intensity as the response variable and dilution steps as the independent variable. For quality control, the resulting curves plot signal intensity against log2 protein

concentration. Final protein concentrations were adjusted for loading using a two-step median-centering process (across both samples and antibodies).

Cytokine array

HER2^{hi} and HER2^{lo} cells were place in mono or co-culture (1:1) for 8 days. Cells were then counted and replated to culture in Opti-MEM (Gibco) without FBS for 24h. Collected supernatant from 3 biological replicates were pooled and analyzed using Proteome Profiler Human XL Cytokine Array (R&D Systems). Imaging was done using a Chemidoc MP device (BioRad) and quantification was performed using ImageJ (RRID:SCR_003070).

Mouse model and tumorigenesis assay

Animal experiments were conducted in accordance with protocol #11-023, approved by the DFCI Institutional Animal Care and Use Committee, and in compliance with NIH guidelines. NOD.Cg-Prkdcscid Il2rgtm1Wjl/SzJ (NSG) mice (RRID:BCBC_4142), aged 5–6 weeks, were purchased from The Jackson Laboratory (RRID:IMSR_GPT:T005557). For mammary fat pad injection, mice were anesthetized with continuous isoflurane inhalation. 1M cells in 50 µL of PBS 50% Matrigel (Corning) were injected in both abdominal mammary glands using insulin syringes and the incision was closed with surgical clips. Post-operative analgesia was provided through the application of topical ropivacaine. Tumor sizes where measure using a caliper. At end point, tumor fluorescence where visualized using ChemiDoc MP imaging system (Bio-Rad).

***In vivo* treatment**

Mice bearing tumors were treated with neratinib (MedChemExpress HKI-272) at 40 mg/kg, administered daily by oral gavage in 200 µL of 0.5% methylcellulose or vehicle control. Trastuzumab deruxtecan (T-DXd, MedChemExpress HY-138298) was administered once weekly via tail vein injection at a dose of 10 mg/kg in 100 µL PBS. For the repeated dosing and

887 combination experiments, reduced dose of T-DXd 1 mg/kg and 5 mg/kg, respectively, were used.
888 G9 (EOAI3402143; MedChemExpress, HY-111408) was administered intraperitoneally at 15 mg/kg
889 in 200 µL every other day. Reversan (MedChemExpress, HY-107643) was administered daily at
890 10 mg/kg. Both G9 and Reversan were prepared in a vehicle consisting of 5% DMSO and 40%
891 PEG400 in PBS and sonicated to ensure proper dissolution.
892
893 **Immunohistostaining**
894 Tissue sections were deparaffinized using xylene and rehydrated in ethanol baths, and antigen
895 retrieval was carried out using Target Retrieval Solution, pH 6 (Agilent) for 20 minutes in a steamer.
896 Slides were incubated in blocking buffer (5% normal goat serum in TBST) for 1h and incubated
897 overnight with indicated primary antibodies in blocking buffer. Secondary antibodies were applied
898 in blocking buffer for 2 hours. Endogenous fluorescence was quenched using a TrueVIEW
899 Autofluorescence Quenching Kit (Vector Laboratories) for 5 minutes. Images were captured using
900 a Nikon ECLIPSE Ti2-E fluorescence microscope. Quantification of PCNA intensity and positivity in
901 the GFP+ or mCherry+ nuclei were performed using ImageJ. The antibodies used are listed in
902 **Supplementary Table S8**.
903
904 **CRISPR Screen**
905 For the pooled genome-wide CRISPR screen, the human CRISPR knockout library H3 (Addgene
906 #133914) generated by Shirley Liu and Myles Brown was used following the provided protocol.
907 Briefly, 120 million 21NT HER2^{lo} cells were infected with the H3 library at a MOI of 0.3, ensuring a
908 high probability that most cells received only one sgRNA. After puromycin selection, the cells were
909 cultured for one month in the presence of with vehicle or T-DXd (500 ng/mL). This experiment was
910 run in biological duplicate, then genomic DNA was extracted using phenol/chloroform/isoamyl
911 alcohol. Library preparation PCR was performed on the genomic DNA to construct the sequencing
912 library as recommended in the provided protocol, increasing the number of cycle for the first PCR

to 24. NextSeq 500 SE 75 sequencing was performed by the Molecular Biology Core Facilitiy at Dana-Farber Cancer Institute (RRID:SCR_009754).

CRISPR data were analyzed using MAGeCK pipeline (RRID:SCR_025016) (25). In brief, raw sequencing data were processed to obtain read counts for each sgRNA after normalization using control sgRNAs of the library. Maximum-likelihood analysis of gene essentialities test (MAGeCK MLE) and sgRNA enriched only in T-DXd (bottom center of the MLE scatter plot) or only in control (top center) were considered. Gene set enrichment analysis of associated hits was performed using MAGeCK GSEA tool. The MAGeCK Flute package was used for data visualization.

Viral Infection and constructs

For virus production, HEK293FT cells (RRID:CVCL_6911) were transfected using Lipofectamine 3000 (Thermo Fisher Scientific) with lentiviral packaging plasmids pMD2.G (RRID:Addgene_12259) and psPAX2 (RRID:Addgene_12260), and indicated plasmids. The viral supernatant was collected 48h hours later, filtered through a 0.45 µm syringe filter and added to cells with 8 µg/mL Polybrene (Millipore). For expression vectors H2B-mCherry (pLV-mpgk-H2B-mCherry-Luc2, designed and made using VectorBuilder) and H2B-GFP (pLV-mpgk-H2B-GFP-Luc2, VectorBuilder), cells were sorted for GFP or mCherry expression 4 days after infection. For CRISPR KO pools, cells were selected 72h later using 2 µg/mL puromycin. To validate the CRISPR screen hits, 2 most depleted guides were selected: ABCC1 (1) AATGTTCAGGGGAAACCGG and (2) TGGGTCCAGGTTCATTCGG, USP9X (1) CTCCTGGCAAACTCACAGG and (2) CAAGTGCTATATCTAACAG, ROSA26 control GGTGATCTAGTATTTCTTG. Guides were cloned in lentiCRISPRv2 (Addgene #52961) following the recommended protocol (65).

Immunoprecipitation and Co-Immunoprecipitation

For immunoprecipitation, cells were lysed using Co-IP buffer (50 mM NaCl, 10 mM Tris pH8, 1% NP-40, 10% glycerol) including phosphatase and protease inhibitors. Lysates were incubated for 1h with 10 μL of anti-USP9X (Santa Cruz sc-365353, RRID:AB_10846088), anti-mouse IgG antibody (Santa Cruz sc-2025, RRID:AB_737182), anti-Human IgG antibody [IG266] (Abcam ab200699, RRID:AB_3698401) and for HER2 IP, cells were treated for 4h with T-DXd (10 μg/mL). Thereafter, lysates were incubated 30 min with Pierce™ Protein A/G Magnetic Beads and washed were made with Co-IP buffer using a magnetic rack. Proteins were then heat-denatured in the presence of β-mercaptoethanol and ran on gels, see Immunoblot section for more information.

Proximity Ligation Assay (PLA)

Cells were fixed with 4% paraformaldehyde (PFA), thoroughly washed with PBS, and then permeabilized using TBST (TBS with 0.2% Triton X-100). After blocking in TBST containing 5% goat serum for 1 hour, cells were incubated with primary antibodies overnight at 4°C. Thereafter, probe hybridization, ligation, and amplification steps were carried out strictly following the manufacturer's instructions (Duolink In Situ, Sigma). The antibodies used are listed in **Supplementary Table S8**. For the negative control, only the HER2 antibody was added, and the rest of the protocol was performed as the other samples. Slides were then mounted with SlowFade containing DAPI (Life Technologies). Imaging was performed using Nikon ECLIPSE Ti2-E fluorescence microscope. Quantifications of the PLA intensity were done with FIJI (RRID:SCR_002285) using a phalloidin staining (Invitrogen) to delimit the cell edges.

Lysosome Enrichment

The lysosome enrichment kit (Thermo Scientific) was used following the company recommendations. Briefly, 8-12M cells were lysed by sonication with Qsonica Q125 (RRID:SCR_019046) in a cooled bath using 2s pulse at 20% amplitude with 3s pause between

each pulse for 1 min. Cell lysates were put on the top of the generated gradient and centrifuge in Beckman ultracentrifuge using SW 55 Ti rotor at 34 600 rpm for 2h at 4°C. Lysosome pellets and total cells were lysed using RIPA buffer and ran on gels as described in the Immunoblot section.

Statistical Analyses

All statistical analyses were performed using GraphPad Prism (RRID:SCR_002798). For single comparisons of normally distributed data, unpaired t-test or Welch's t-test (when the assumption of equal variance was implausible) were used. For comparisons involving more than two groups, one-way or two-way ANOVA was performed with correction for multiple comparisons. A Chi-square test without Yates' correction was used to assess the association between treatment conditions and *ERBB2* amplification status across 675–1,421 cells per resistant cell lines. Furthermore, Pearson's correlation coefficient (two-tailed) was calculated to evaluate the relationship between drug IC50 values and the proportion of $HER2^{lo}$ cells. Survival analyses were assessed using the log-rank (Mantel–Cox) test. All statistical analyses were conducted with a 95% confidence interval, and corresponding P-values ($P < 0.05$ considered significant) were reported for each experiment.

Data availability

All data needed to evaluate the conclusions in the paper are present in the paper and/or the Supplementary Information. All raw and processed RNA-seq and scRNA-seq data were deposited to NCBI GEO database under accession number GSE300628. RNA-seq data from NCT02326974 clinical trial (9,16) are available under GSE243375. This study did not generate custom code.

AUTHOR CONTRIBUTIONS

M.-A. Goyette: Conceptualization, methodology, investigation, data curation, formal analysis, visualization, supervision, funding acquisition, writing–original draft, writing– review and editing. **C.**

Graser: Investigation, methodology, formal analysis, visualization, writing– review and editing. **M. Seehawer**: Investigation, formal analysis, writing– review and editing. **A. Patmanidis**: Investigation, data curation. **E.R. Jimenez**: Formal analysis, writing– review and editing. **A. Kamat**: Investigation, data curation. **A. Fassl**: Investigation, data curation. **P. Foidart**: Investigation, writing– review and editing. **Z. Li**: Formal analysis, writing– review and editing. **A. James**: Investigation. **P. Sicinski**: supervision, writing–review and editing. **F. Michor**: Methodology, supervision, funding acquisition, writing–review and editing. **K. Polyak**: Conceptualization, methodology, resources, supervision, funding acquisition, writing–original draft, writing–review and editing.

ACKNOWLEDGEMENTS

We are grateful to members of our laboratory for their valuable feedback on the manuscript and for engaging in thoughtful and stimulating discussions throughout the study. We also thank Charles Coulombe for his contribution to the analysis of the spatial data, the Dana-Farber Cancer Institute Flow Cytometry, Molecular Biology, and Molecular Imaging Core Facilities, and the Rodent Histopathology at Harvard Medical School for their outstanding service. This work utilized an Illumina NovaSeq X Plus that was purchased with funding from a National Institutes of Health SIG grant 1S10OD036228-01. The Functional Proteomics Reverse Phase Protein Array (RPPA) Core Facility receives partial support from the National Cancer Institute under grant P30CA016672 to MD Anderson Cancer Center. The research reported in this publication was not directly funded through the grant P30CA016672 to MD Anderson Cancer Center and is not within the scope of such grant. This research was supported by the National Cancer Institute R35 CA197623 (K. Polyak), SPORE in Breast Cancer P50CA168504 (K. Polyak), P01 CA250959 (P. Sicinski), R35 CA305086 (P. Sicinski), the Canadian Institutes of Health Research 202110MFE-472650-242151 and Grant 1505135 from the Cancer Research Society and BMO Financial Group (M.-A. Goyette).

REFERENCES

1. Kallioniemi OP, Kallioniemi A, Kurisu W, Thor A, Chen LC, Smith HS*, et al.* ERBB2 amplification in breast cancer analyzed by fluorescence in situ hybridization. Proc Natl Acad Sci U S A **1992**;89(12):5321-5 doi 10.1073/pnas.89.12.5321.
2. Slamon DJ, Godolphin W, Jones LA, Holt JA, Wong SG, Keith DE*, et al.* Studies of the HER-2/neu proto-oncogene in human breast and ovarian cancer. Science **1989**;244(4905):707-12 doi 10.1126/science.2470152.
3. Hayes DF. HER2 and Breast Cancer — A Phenomenal Success Story. New England Journal of Medicine **2019**;381(13):1284-6 doi doi:10.1056/NEJMcibr1909386.
4. Minckwitz Gv, Procter M, Azambuja Ed, Zardavas D, Benyunes M, Viale G*, et al.* Adjuvant Pertuzumab and Trastuzumab in Early HER2-Positive Breast Cancer. New England Journal of Medicine **2017**;377(2):122-31 doi doi:10.1056/NEJMoa1703643.
5. O'Meara TA, Tarantino P, Morganti S, Schlam I, Garrido-Castro AC, Tolaney SM. Antibody-Drug Conjugates in Breast Cancer: The Road Towards Biologically-Informed Selection and Sequencing. Curr Oncol Rep **2025**;27(1):68-79 doi 10.1007/s11912-024-01628-0.
6. Schlam I, Tarantino P, Tolaney SM. Overcoming Resistance to HER2-Directed Therapies in Breast Cancer. Cancers (Basel) **2022**;14(16) doi 10.3390/cancers14163996.
7. Khongorzul P, Ling CJ, Khan FU, Ihsan AU, Zhang J. Antibody–Drug Conjugates: A Comprehensive Review. Molecular Cancer Research **2020**;18(1):3-19 doi 10.1158/1541-7786.Mcr-19-0582.
8. Colombo R, Tarantino P, Rich JR, LoRusso PM, de Vries EGE. The Journey of Antibody–Drug Conjugates: Lessons Learned from 40 Years of Development. Cancer Discovery **2024**;14(11):2089-108 doi 10.1158/2159-8290.Cd-24-0708.
9. Filho OM, Viale G, Stein S, Trippa L, Yardley DA, Mayer IA*, et al.* Impact of HER2 Heterogeneity on Treatment Response of Early-Stage HER2-Positive Breast Cancer: Phase II Neoadjuvant Clinical Trial of T-DM1 Combined with Pertuzumab. Cancer Discov **2021**;11(10):2474-87 doi 10.1158/2159-8290.Cd-20-1557.
10. Lee HJ, Seo AN, Kim EJ, Jang MH, Suh KJ, Ryu HS*, et al.* HER2 heterogeneity affects trastuzumab responses and survival in patients with HER2-positive metastatic breast cancer. Am J Clin Pathol **2014**;142(6):755-66 doi 10.1309/ajcpirl4guvgk3yx.
11. Tanei T, Seno S, Sota Y, Hatano T, Kitahara Y, Abe K*, et al.* High HER2 Intratumoral Heterogeneity Is a Predictive Factor for Poor Prognosis in Early-Stage and Locally Advanced HER2-Positive Breast Cancer. Cancers **2024**;16(5):1062.
12. Rye IH, Trinh A, Sætersdal AB, Nebdal D, Lingjærde OC, Almendro V*, et al.* Intratumor heterogeneity defines treatment-resistant HER2+ breast tumors. Molecular Oncology **2018**;12(11):1838-55 doi https://doi.org/10.1002/1878-0261.12375.
13. Wolff AC, Hammond ME, Hicks DG, Dowsett M, McShane LM, Allison KH*, et al.* Recommendations for human epidermal growth factor receptor 2 testing in breast cancer: American Society of Clinical Oncology/College of American Pathologists clinical practice guideline update. J Clin Oncol **2013**;31(31):3997-4013 doi 10.1200/jco.2013.50.9984.
14. DePristo MA, Banks E, Poplin R, Garimella KV, Maguire JR, Hartl C*, et al.* A framework for variation discovery and genotyping using next-generation DNA sequencing data. Nature Genetics **2011**;43(5):491-8 doi 10.1038/ng.806.
15. Ogitani Y, Hagihara K, Oitate M, Naito H, Agatsuma T. Bystander killing effect of DS-8201a, a novel anti-human epidermal growth factor receptor 2 antibody-drug conjugate, in tumors with human epidermal growth factor receptor 2 heterogeneity. Cancer Sci **2016**;107(7):1039-46 doi 10.1111/cas.12966.
16. Li Z, Metzger Filho O, Viale G, dell'Orto P, Russo L, Goyette MA*, et al.* HER2 heterogeneity and treatment response-associated profiles in HER2-positive breast cancer in the NCT02326974 clinical trial. J Clin Invest **2024**;134(7) doi 10.1172/jci176454.

17. Band V, Zajchowski D, Swisshelm K, Trask D, Kulesa V, Cohen C*, et al.* Tumor progression in four mammary epithelial cell lines derived from the same patient. Cancer Res **1990**;50(22):7351-7.
18. Gazdar AF, Kurvari V, Virmani A, Gollahon L, Sakaguchi M, Westerfield M*, et al.* Characterization of paired tumor and non-tumor cell lines established from patients with breast cancer. Int J Cancer **1998**;78(6):766-74 doi 10.1002/(sici)1097-0215(19981209)78:6<766::aid-ijc15>3.0.co;2-l.
19. Perou CM, Sorlie T, Eisen MB, van de Rijn M, Jeffrey SS, Rees CA*, et al.* Molecular portraits of human breast tumours. Nature **2000**;406(6797):747-52 doi 10.1038/35021093.
20. Janiszewska M, Stein S, Metzger Filho O, Eng J, Kingston NL, Harper NW*, et al.* The impact of tumor epithelial and microenvironmental heterogeneity on treatment responses in HER2+ breast cancer. JCI Insight **2021**;6(11) doi 10.1172/jci.insight.147617.
21. Freedman RA, Heiling HM, Li T, Trapani D, Tayob N, Smith KL*, et al.* Neratinib and ado-trastuzumab emtansine for pretreated and untreated human epidermal growth factor receptor 2 (HER2)-positive breast cancer brain metastases: Translational Breast Cancer Research Consortium trial 022. Ann Oncol **2024**;35(11):993-1002 doi 10.1016/j.annonc.2024.07.245.
22. Li BT, Michelini F, Misale S, Cocco E, Baldino L, Cai Y*, et al.* HER2-Mediated Internalization of Cytotoxic Agents in ERBB2 Amplified or Mutant Lung Cancers. Cancer Discovery **2020**;10(5):674-87 doi 10.1158/2159-8290.Cd-20-0215.
23. Gutierrez C, Al'Khafaji AM, Brenner E, Johnson KE, Gohil SH, Lin Z*, et al.* Multifunctional barcoding with ClonMapper enables high-resolution study of clonal dynamics during tumor evolution and treatment. Nat Cancer **2021**;2(7):758-72 doi 10.1038/s43018-021-00222-8.
24. Pal B, Chen Y, Vaillant F, Capaldo BD, Joyce R, Song X*, et al.* A single-cell RNA expression atlas of normal, preneoplastic and tumorigenic states in the human breast. Embo j **2021**;40(11):e107333 doi 10.15252/embj.2020107333.
25. Li W, Xu H, Xiao T, Cong L, Love MI, Zhang F*, et al.* MAGeCK enables robust identification of essential genes from genome-scale CRISPR/Cas9 knockout screens. Genome Biology **2014**;15(12):554 doi 10.1186/s13059-014-0554-4.
26. Borst P, Evers R, Kool M, Wijnholds J. A Family of Drug Transporters: the Multidrug Resistance-Associated Proteins. JNCI: Journal of the National Cancer Institute **2000**;92(16):1295-302 doi 10.1093/jnci/92.16.1295.
27. Loganzo F, Tan X, Sung M, Jin G, Myers JS, Melamud E*, et al.* Tumor cells chronically treated with a trastuzumab-maytansinoid antibody-drug conjugate develop varied resistance mechanisms but respond to alternate treatments. Mol Cancer Ther **2015**;14(4):952-63 doi 10.1158/1535-7163.Mct-14-0862.
28. Janiszewska M, Liu L, Almendro V, Kuang Y, Paweletz C, Sakr RA*, et al.* In situ single-cell analysis identifies heterogeneity for PIK3CA mutation and HER2 amplification in HER2-positive breast cancer. Nat Genet **2015**;47(10):1212-9 doi 10.1038/ng.3391.
29. Fehm T, Cottone F, Dunton K, André F, Krop I, Park YH*, et al.* Trastuzumab deruxtecan versus treatment of physician's choice in patients with HER2-positive metastatic breast cancer (DESTINY-Breast02): patient-reported outcomes from a randomised, open-label, multicentre, phase 3 trial. Lancet Oncol **2024**;25(5):614-25 doi 10.1016/s1470-2045(24)00128-1.
30. Modi S, Jacot W, Yamashita T, Sohn J, Vidal M, Tokunaga E*, et al.* Trastuzumab Deruxtecan in Previously Treated HER2-Low Advanced Breast Cancer. N Engl J Med **2022**;387(1):9-20 doi 10.1056/NEJMoa2203690.
31. Tolaney SM, Jiang Z, Zhang Q, Barroso-Sousa R, Park YH, Rimawi MF*, et al.* Trastuzumab deruxtecan (T-DXd) + pertuzumab (P) vs taxane + trastuzumab + pertuzumab (THP) for first-line (1L) treatment of patients (pts) with human epidermal growth factor receptor 2–positive (HER2+) advanced/metastatic breast cancer (a/mBC): Interim results from

DESTINY-Breast09. Journal of Clinical Oncology **2025**;43(17_suppl):LBA1008-LBA doi 10.1200/JCO.2025.43.17_suppl.LBA1008.
32. Chen W, Gupta A, Mai N, Nag S, Lau JS, Singh S, *et al.* Trastuzumab Deruxtecan Resistance via Loss of HER2 Expression and Binding. Cancer Discov **2026**;16(2):235-49 doi 10.1158/2159-8290.Cd-25-0647.
33. Guidi L, Pellizzari G, Tarantino P, Valenza C, Curigliano G. Resistance to Antibody-Drug Conjugates Targeting HER2 in Breast Cancer: Molecular Landscape and Future Challenges. Cancers (Basel) **2023**;15(4) doi 10.3390/cancers15041130.
34. Fletcher JI, Williams RT, Henderson MJ, Norris MD, Haber M. ABC transporters as mediators of drug resistance and contributors to cancer cell biology. Drug Resist Updat **2016**;26:1-9 doi 10.1016/j.drup.2016.03.001.
35. Yu M, Ocana A, Tannock IF. Reversal of ATP-binding cassette drug transporter activity to modulate chemoresistance: why has it failed to provide clinical benefit? Cancer Metastasis Rev **2013**;32(1-2):211-27 doi 10.1007/s10555-012-9402-8.
36. Dupont S, Mamidi A, Cordenonsi M, Montagner M, Zacchigna L, Adorno M, *et al.* FAM/USP9x, a deubiquitinating enzyme essential for TGFbeta signaling, controls Smad4 monoubiquitination. Cell **2009**;136(1):123-35 doi 10.1016/j.cell.2008.10.051.
37. Savio Michol G, Wollscheid N, Cavallaro E, Algisi V, Di Fiore Pier P, Sigismund S, *et al.* USP9X Controls EGFR Fate by Deubiquitinating the Endocytic Adaptor Eps15. Current Biology **2016**;26(2):173-83 doi https://doi.org/10.1016/j.cub.2015.11.050.
38. Li L, Liu T, Li Y, Wu C, Luo K, Yin Y, *et al.* The deubiquitinase USP9X promotes tumor cell survival and confers chemoresistance through YAP1 stabilization. Oncogene **2018**;37(18):2422-31 doi 10.1038/s41388-018-0134-2.
39. Jaiswal A, Murakami K, Elia A, Shibahara Y, Done SJ, Wood SA, *et al.* Therapeutic inhibition of USP9x-mediated Notch signaling in triple-negative breast cancer. Proceedings of the National Academy of Sciences **2021**;118(38):e2101592118 doi doi:10.1073/pnas.2101592118.
40. Schwickart M, Huang X, Lill JR, Liu J, Ferrando R, French DM, *et al.* Deubiquitinase USP9X stabilizes MCL1 and promotes tumour cell survival. Nature **2010**;463(7277):103-7 doi 10.1038/nature08646.
41. Wolfsperger F, Hogh-Binder SA, Schittenhelm J, Psaras T, Ritter V, Bornes L, *et al.* Deubiquitylating enzyme USP9x regulates radiosensitivity in glioblastoma cells by Mcl-1-dependent and -independent mechanisms. Cell Death & Disease **2016**;7(1):e2039-e doi 10.1038/cddis.2015.405.
42. Engel K, Rudelius M, Slawska J, Jacobs L, Ahangarian Abhari B, Altmann B, *et al.* USP9X stabilizes XIAP to regulate mitotic cell death and chemoresistance in aggressive B-cell lymphoma. EMBO Molecular Medicine **2016**;8(8):851-62 doi https://doi.org/10.15252/emmm.201506047.
43. Marx C, Held JM, Gibson BW, Benz CC. ErbB2 trafficking and degradation associated with K48 and K63 polyubiquitination. Cancer Res **2010**;70(9):3709-17 doi 10.1158/0008-5472.Can-09-3768.
44. Wei Q, Yang T, Zhang Z, Wang F, Yang Y, Zhu J, *et al.* Perivascular Niche-Resident Alveolar Macrophages Promote Interstitial Pneumonitis Related to Trastuzumab Deruxtecan Treatment. Cancer Res **2025**;85(11):2081-99 doi 10.1158/0008-5472.Can-24-2021.
45. Mosele F, Deluche E, Lusque A, Le Bescond L, Filleron T, Pradat Y, *et al.* Trastuzumab deruxtecan in metastatic breast cancer with variable HER2 expression: the phase 2 DAISY trial. Nature Medicine **2023**;29(8):2110-20 doi 10.1038/s41591-023-02478-2.
46. Vaz Batista M, Pérez-García JM, Cortez P, Garrigós L, Fernández-Abad M, Gion M, *et al.* Trastuzumab deruxtecan in patients with previously treated HER2-low advanced breast cancer and active brain metastases: the DEBBRAH trial. ESMO Open **2024**;9(9):103699 doi 10.1016/j.esmoop.2024.103699.

47. Shen S, Ma W, Brown D, Da Cruz Paula A, Zhou Q, Iaosonos A*, et al.* HER2 Genetic Intratumor Heterogeneity Is Associated With Resistance to Trastuzumab and Trastuzumab Emtansine Therapy in Recurrent High-Grade Endometrial Cancer. Mod Pathol **2023**;36(11):100299 doi 10.1016/j.modpat.2023.100299.
48. Fukai S, Nakajima S, Saito M, Saito K, Kase K, Nakano H*, et al.* Down-regulation of stimulator of interferon genes (STING) expression and CD8(+) T-cell infiltration depending on HER2 heterogeneity in HER2-positive gastric cancer. Gastric Cancer **2023**;26(6):878-90 doi 10.1007/s10120-023-01417-x.
49. McLaren W, Gil L, Hunt SE, Riat HS, Ritchie GRS, Thormann A*, et al.* The Ensembl Variant Effect Predictor. Genome Biology **2016**;17(1):122 doi 10.1186/s13059-016-0974-4.
50. Talevich E, Shain AH, Botton T, Bastian BC. CNVkit: Genome-Wide Copy Number Detection and Visualization from Targeted DNA Sequencing. PLoS Comput Biol **2016**;12(4):e1004873 doi 10.1371/journal.pcbi.1004873.
51. Cornwell M, Vangala M, Taing L, Herbert Z, Köster J, Li B*, et al.* VIPER: Visualization Pipeline for RNA-seq, a Snakemake workflow for efficient and complete RNA-seq analysis. BMC Bioinformatics **2018**;19(1):135 doi 10.1186/s12859-018-2139-9.
52. Dobin A, Davis CA, Schlesinger F, Drenkow J, Zaleski C, Jha S*, et al.* STAR: ultrafast universal RNA-seq aligner. Bioinformatics **2013**;29(1):15-21 doi 10.1093/bioinformatics/bts635.
53. Wang L, Wang S, Li W. RSeQC: quality control of RNA-seq experiments. Bioinformatics **2012**;28(16):2184-5 doi 10.1093/bioinformatics/bts356.
54. Love MI, Huber W, Anders S. Moderated estimation of fold change and dispersion for RNA-seq data with DESeq2. Genome Biol **2014**;15(12):550 doi 10.1186/s13059-014-0550-8.
55. Subramanian A, Tamayo P, Mootha VK, Mukherjee S, Ebert BL, Gillette MA*, et al.* Gene set enrichment analysis: a knowledge-based approach for interpreting genome-wide expression profiles. Proc Natl Acad Sci U S A **2005**;102(43):15545-50 doi 10.1073/pnas.0506580102.
56. Liberzon A, Birger C, Thorvaldsdóttir H, Ghandi M, Mesirov JP, Tamayo P. The Molecular Signatures Database (MSigDB) hallmark gene set collection. Cell Syst **2015**;1(6):417-25 doi 10.1016/j.cels.2015.12.004.
57. Aouad P, Zhang Y, De Martino F, Stibolt C, Ali S, Ambrosini G*, et al.* Epithelial-mesenchymal plasticity determines estrogen receptor positive breast cancer dormancy and epithelial reconversion drives recurrence. Nature Communications **2022**;13(1):4975 doi 10.1038/s41467-022-32523-6.
58. Li CM-C, Shapiro H, Tsiobikas C, Selfors LM, Chen H, Rosenbluth J*, et al.* Aging-Associated Alterations in Mammary Epithelia and Stroma Revealed by Single-Cell RNA Sequencing. Cell Reports **2020**;33(13) doi 10.1016/j.celrep.2020.108566.
59. Satija R, Farrell JA, Gennert D, Schier AF, Regev A. Spatial reconstruction of single-cell gene expression data. Nature Biotechnology **2015**;33(5):495-502 doi 10.1038/nbt.3192.
60. Jin S, Guerrero-Juarez CF, Zhang L, Chang I, Ramos R, Kuan C-H*, et al.* Inference and analysis of cell-cell communication using CellChat. Nature Communications **2021**;12(1):1088 doi 10.1038/s41467-021-21246-9.
61. Martin M. Cutadapt removes adapter sequences from high-throughput sequencing reads. EMBnet Journal **2011**; 17(1):3 doi 10.14806/ej.17.1.200.
62. Miller CA, McMichael J, Dang HX, Maher CA, Ding L, Ley TJ*, et al.* Visualizing tumor evolution with the fishplot package for R. BMC Genomics **2016**;17(1):880 doi 10.1186/s12864-016-3195-z.
63. Siwak DR, Li J, Akbani R, Liang H, Lu Y. Analytical Platforms 3: Processing Samples via the RPPA Pipeline to Generate Large-Scale Data for Clinical Studies. Adv Exp Med Biol **2019**;1188:113-47 doi 10.1007/978-981-32-9755-5_7.

64. Shehwana H, Kumar SV, Melott JM, Rohrdanz MA, Wakefield C, Ju Z, *et al.* RPPA SPACE: an R package for normalization and quantitation of Reverse-Phase Protein Array data. Bioinformatics **2022**;38(22):5131-3 doi 10.1093/bioinformatics/btac665.
65. Sanjana NE, Shalem O, Zhang F. Improved vectors and genome-wide libraries for CRISPR screening. Nature Methods **2014**;11(8):783-4 doi 10.1038/nmeth.3047.

FIGURE LEGENDS

Figure 1. Generation and characterization of HER2 heterogeneous models. A, Flow cytometry histograms (left) and dot plots (right) showing cell surface HER2 protein levels across HER2+ breast cancer cell lines. **B**, Flow cytometry histograms showing cell surface HER2 protein levels in sorted $HER2^{hi}$ and $HER2^{lo}$ subpopulations within the indicated cell lines. **C,** Immunoblot analysis of HER2 protein levels in $HER2^{hi}$ and $HER2^{lo}$ cells. Tubulin was used as loading control. **D,** FISH analysis of *ERBB2* and CEP17 copy numbers in $HER2^{hi}$ and $HER2^{lo}$ cells derived from the indicated cell lines. Scale bar, 25 μm. **E,** Copy number variation (CNV) plots of paired $HER2^{hi}$ and $HER2^{lo}$ cells. Coloring reflects CNV detected in both (gray), or unique to $HER2^{hi}$ (red) or $HER2^{lo}$ (blue) cells. **F,** Plot depicting the presence of point mutations in oncogenes and tumor suppressors commonly mutated in breast cancer in paired $HER2^{hi}$ and $HER2^{lo}$ cells. **G,** Plots depicting PAM50 subtype probability scores of paired $HER2^{hi}$ and $HER2^{lo}$ cells assessed by RNA-seq. **H,** Graphs showing the fraction of $HER2^{hi}$ and $HER2^{lo}$ cancer cells positive for the indicated subtype-specific markers in HER2+ breast tumors (n=20 patients) based on cyclic immunofluorescence (20), t-test.

Figure 2. The effect of HER2-targeting agents on $HER2^{hi}$ and $HER2^{lo}$ population. A, Dose-response of the indicated compounds tested at various concentrations in parental 21NT and $HER2^{hi}$ and $HER2^{lo}$ derivates. Comparison to $HER2^{hi}$ cells, p-values in blue ($HER2^{lo}$) or purple (parental). **B,** Immunoblot analysis of EGFR, HER2, and downstream signaling pathway components in $HER2^{hi}$ and $HER2^{lo}$ cells treated with vehicle or neratinib. **C,** Flow cytometry analysis of $HER2^{lo}$ subpopulation of patient derived organoids from HER2 heterogeneous tumor T537 treated with T-DXd or neratinib. **D**, FISH analysis of *ERBB2* and CEP17 copy numbers in control 21NT cells and derivates resistant to T-DXd (TDR), T-DM1 (TMR), neratinib (NR), or

tucatinib (TR). Bar plot depicts quantification of FISH signal in 675-1421 cells per condition. Chi-square without Yates correction. Scale bar 25 μm. **E,** Principal component analysis plot of RNA-seq profiles of HCC1954 control cells, $HER2^{hi}$ and $HER2^{lo}$ subpopulations, and resistant derivates. **F,** Bar graph showing Euclidean distances between PC1 and PC2 of the indicated RNA-seq samples from panel **E**. **G,** Dose-response of the indicated compounds tested at various concentrations in control 21NT cells and resistant derivates. Comparison to vehicle control cells, p-value colored for the different cells as indicated). Data are presented as mean ± SEM, n = 3, two-way ANOVA (panels **A** and **G**).

Figure 3. Subclonal dynamics of $HER2^{hi}$ and $HER2^{lo}$ cells during evolution to resistance in mono- or in co-cultures. A, Plots depicting viable cell numbers of HCC1954 $HER2^{hi}$ and $HER2^{lo}$ cells grown separately in monoculture or together in co-culture in the presence of DMSO, T-DXd, T-DM1, neratinib or tucatinib. **B,** Heatmap depicting the relative bystander effect of T-DXd in a panel of $HER2^{lo}$ or TNBC cells in co-culture with different $HER2^{hi}$ cells (mean of n = 3). **C,** Dose-response of DXd tested at various concentrations in different $HER2^{lo}$ and TNBC cells. **D,** Schematic outline of the experiment where HCC1954 $HER2^{hi}$ and $HER2^{lo}$ cells are infected with the Clonmapper library and barcoded cells are grown in mono- or co-culture in the presence of DMSO, T-DXd or neratinib. **E,** Bar plot depicting the number of days per passage in the indicated conditions, including the ratio of $HER2^{hi}$ and $HER2^{lo}$ cells in initially 1:1 co-culture. **F,** Shannon entropy measuring barcode diversity over different passages of $HER2^{hi}$ and $HER2^{lo}$ cells growing in mono- or co-cultures in the presence of DMSO, neratinib or T-DXd. **G,** Bar plot illustrating the number of barcodes remaining in the top 90% of $HER2^{hi}$ and $HER2^{lo}$ cells after 10 passages (DMSO and neratinib) or 4 passages (T-DXd). One-way ANOVA comparing all conditions to DMSO neratinib ($HER2^{hi}$, $p<0.0001$, $HER2^{lo}$, $p<0.0001$) and T-DXd, ($HER2^{hi}$, $p<0.0001$, $HER2^{lo}$ monoculture, $p=0.0070$, and co-culture $p<0.0001$). **H,** Stacked barplot depicting the relative proportion of barcodes within $HER2^{hi}$ and $HER2^{lo}$ cells at final passage. Each barcode in the top 30

is represented by one color across each panel and gray represents all other barcodes in the population. Data are presented as mean, n = 3, two-way ANOVA (panels **A, C** and **F**).

Figure 4. The impact of HER2 heterogeneity on tumorigenesis and treatment responses in vivo. A, Tumor growth of mammary fat pad injection of 21NT homogeneous $HER2^{hi}$ or $HER2^{lo}$, and heterogeneous 1:1 mix (n=5). **B,** Immunohistochemistry for mCherry ($HER2^{hi}$), GFP ($HER2^{lo}$) and HER2 reveals that $HER2^{hi}$, $HER2^{lo}$ retain their different HER2 levels in heterogeneous tumors *in vivo.* Scale bar, 50 µm. **C,D,** Stacked barplot representing the neighborhood composition of $HER2^{hi}$ and $HER2^{lo}$ cells in 21NT HER2 heterogeneous tumors (**C**, n=5 tumors) or human tumors from the CycIF of (20) (**D**, n=20 patients), t-test (p-value in red for $HER2^{hi}$ and blue for $HER2^{lo}$). **E,** PCNA, mCherry ($HER2^{hi}$) and GFP ($HER2^{lo}$) staining on 21NT HER2 heterogeneous tumors. Scale bar, 50 µm. **F,G,** Quantification of staining for PCNA staining proliferation marker in $HER2^{hi}$ and $HER2^{lo}$ cells in HER2 heterogenous 21NT (**F**, n=5) or human tumors (20) (**G**, n=20 patients), t-test. **H,I,** UMAP of scRNA-seq of all cells from human HER2 heterogenous breast tumors T537 and T565. Clusters are colored by samples (**H**) and by gene module scores (**I**). **J,** CellChat analysis of scRNA-seq data depicting the amount of incoming and outgoing interactions of every cell type**. K,** Plot presenting the pathways of the overall signals comparing $HER2^{lo}$ and $HER2^{hi}$ cell populations **L,** Presence of $PDPN^{+}$ stromal cells in the neighborhood of $HER2^{hi}$ and $HER2^{lo}$ cells (n=20 patients, t-test). **M,** Schematic depicting the *in vivo* experiment set up where 21NT homogeneous and heterogeneous tumors are treated with neratinib or T-DXd. **N,** Curve of changes in tumor size under treatment with neratinib or T-DXd. n = 9-10, two-way ANOVA. **O,** Fluorescence pictures of tumors after 2 weeks treatment showing $HER2^{hi}$ cells in red and $HER2^{lo}$ cells in blue. Scale bar, 1 cm. **P,** Quantification by flow cytometry of the composition of heterogeneous tumors in $HER2^{hi}$ and $HER2^{lo}$ cells after 2 weeks of treatment. n=5, One-way ANOVA. **Q,** Schematic depicting the survival assay where tumors are treated for 2 weeks with T-DXd or neratinib and mice are followed until tumor recurrence. **R,** Tumor growth and recurrence of homogeneous and heterogeneous

tumors upon T-DXd or neratinib treatment. n=10-12 tumors, two-way ANOVA. **S,** Survival curves showing time to tumor volume endpoint in mice treated with indicated treatments comparing homogeneous and heterogeneous tumor-bearing mice. n=5-6 mice, Long-rank (Mantel-Cox) test. **T,** Quantification by flow cytometry of the composition of heterogeneous tumors in $HER2^{hi}$ and $HER2^{lo}$ cells after recurrence. n=5, One-way ANOVA. Data are presented as mean ± SEM (panels **C-D, F-G, L, N, P** and **T**).

Figure 5. CRISPR KO cellular viability screen with T-DXd in co-cultures. A, Schematic showing 21NT $HER2^{lo}$ cells infected with Cas9 and whole genome CRISPR KO library and put in co-culture with $HER2^{hi}$ cells in the presence or not of T-DXd for 1 month. **B,** Bubble plot illustrating the enrichment in KEGG pathways of the CRISPR hits linked to resistance (red) and synthetic lethality (blue). **C,** Scatter plot from mle analysis depicting hits from the CRISPR screen only changed in the T-DXd condition linked to resistance or synthetic lethality. **D,** Histogram showing cell count normalized to the untreated control with or without T-DXd for 10 days upon genetic (sg*ABCC1*, sg*USP9X*) or pharmacologic (reversan or biricodar, G9 or FT709) inhibition of ABCC1 or USP9X in 21NT $HER2^{lo}$ cells. **E,** Treatment with G9, FT709, reversan or biricodar increased T-DXd effect in 21NT TDR after 10 days. **F,** Bar graph showing cell counts normalized to the untreated control with or without DXd upon genetic (sg*ABCC1*) or pharmacologic (reversan or biricodar) inhibition of ABCC1 in 21NT $HER2^{lo}$ cells. **G,** ABCC1 KO in 21NT $HER2^{lo}$ cells increases the bystander effect of T-DXd in co-culture with HCC1954 $HER2^{hi}$ cells. **H,** Schematic outline of the survival assay experiment. **I,** Graph illustrating the volume of individual tumors during the indicated treatment. n = 8-10 tumors, two-way ANOVA. **J,** Kaplan-Meier plot showing time to tumor volume endpoint in mice with the indicated treatments (n=4-5 mice, Long-rank (Mantel-Cox) test). Data are presented as mean ± SEM, n = 3, One-way ANOVA (**D-G**).

Figure 6. The effect of USP9X inhibition on lysosomal targeting of HER2 and response to T-DXd. A, Immunoblot analysis of HER2 immunoprecipitation (IP) probed for ubiquitin (Ub) shows an increase of HER2 ubiquitination upon USP9X inhibition in the presence of T-DXd in 21NT HER2^{lo} cells. **B,** Co-immunoprecipitation experiments show an interaction between USP9X and HER2. **C,** Proximity Ligation Assay (PLA) between HER2 and USP9X in 21NT HER2^{lo} cells treated with vehicle or T-DXd. Scale: 20 μm. Quantification of PLA intensity per cell. 15 cells from each replicate. **D,** Immunoblot analysis of HER2 levels of 21NT HER2^{lo} cells after treatment with T-DXd upon USP9X inhibition. **E-F,** Cycloheximide chase for HER2 in 21NT HER2^{lo} cells upon T-DXd treatment with USP9X inhibition, including the quantification of HER2 levels. n=3, Two-way ANOVA. **G,** PLA experiment between HER2 and LAMP1 in 21NT HER2^{lo} cells treated with T-DXd and FT709. **H,** Quantification of PLA intensity per cell. 15 cells from each replicate. **I,** Immunoblot of total cell lysate (TCL) and lysosome enriched fraction of 21NT HER2^{lo} cells treated as in panel G. LAMP1 was used as a lysosome marker, CTCF as nuclear marker and TUFM as a mitochondria marker, confirming lysosome enrichment. **J,** *USP9X* mRNA expression in human tumors before and after T-DM1/pertuzumab neoadjuvant treatment from NCT02326974 clinical trial (9,16), separated by pCR or no pCR, and No HET or HET. **K,** Schematic depicting the survival experiment where 21NT HER2 heterogeneous tumors are treated with one dose of T-DXd, G9 or both. **L,** Tumor growth of individual tumors following indicated treatment. n = 8-10 tumors, two-way ANOVA. **M,** Survival curves showing time to tumor volume endpoint in mice treated with indicated treatments. n=4-5 mice, Long-rank (Mantel-Cox) test. **N,** Graphical summary showing the role of USP9X and ABCC1 in sensitivity to T-T-DXd. Data are presented as mean ± SEM, n = 3, one-way ANOVA (**C, H** and **J**) or two-way ANOVA (**E** and **L**).

Fig. 1

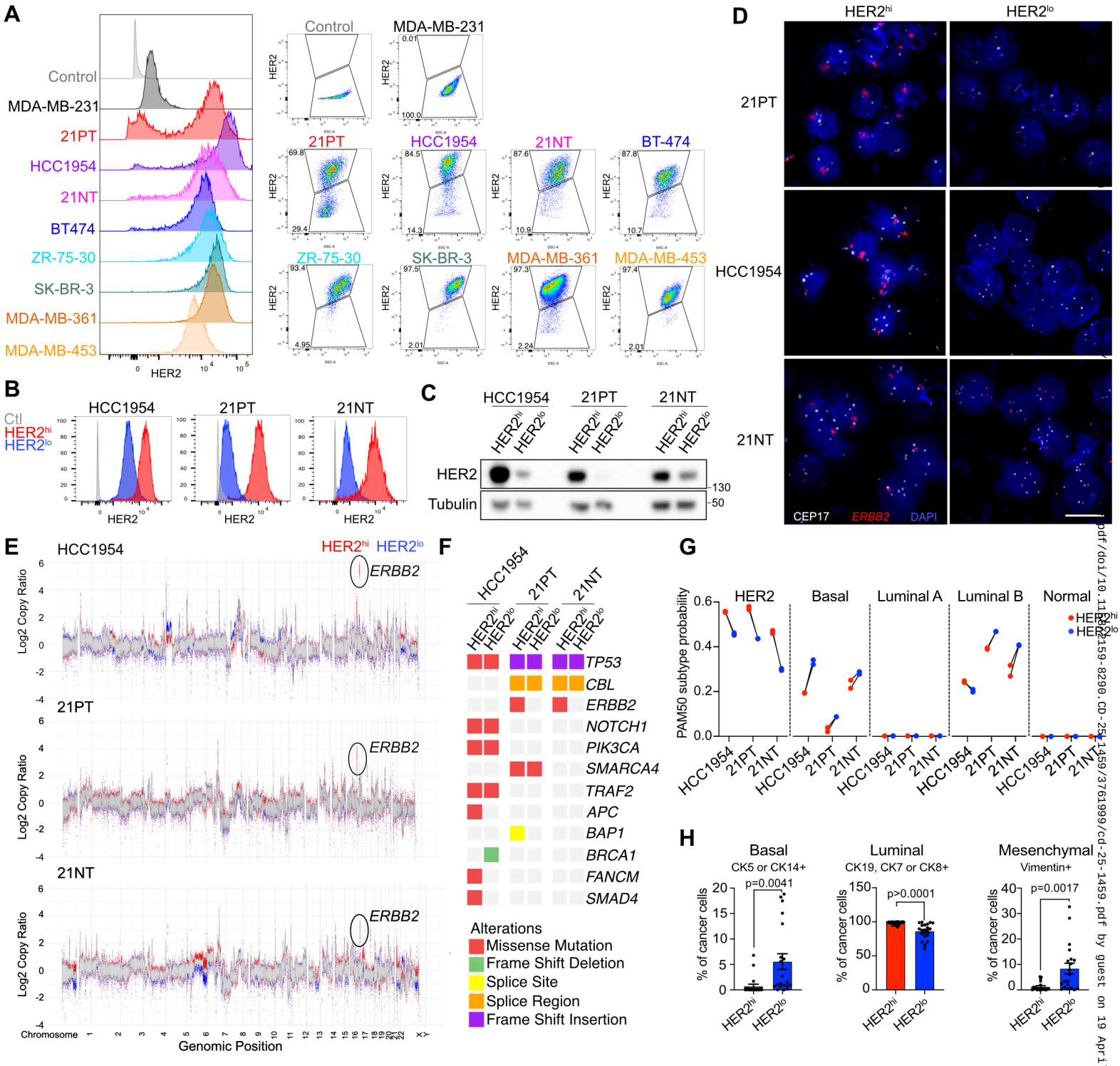

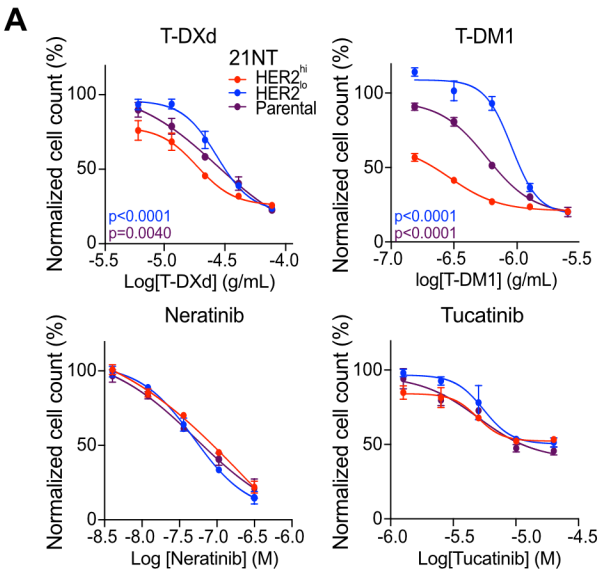

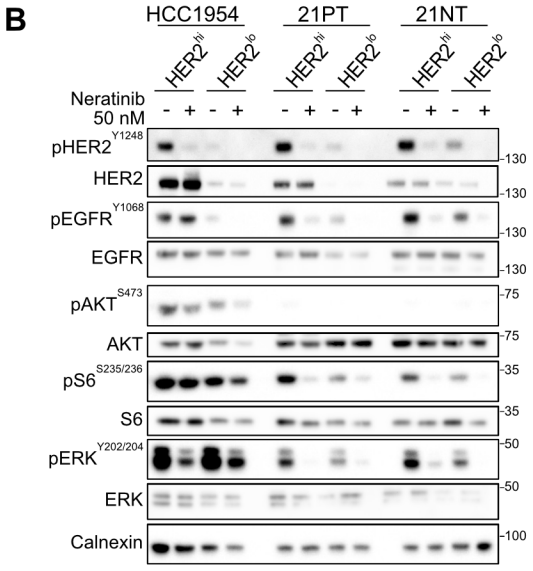

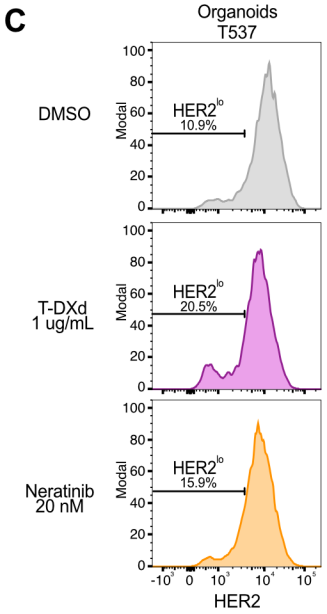

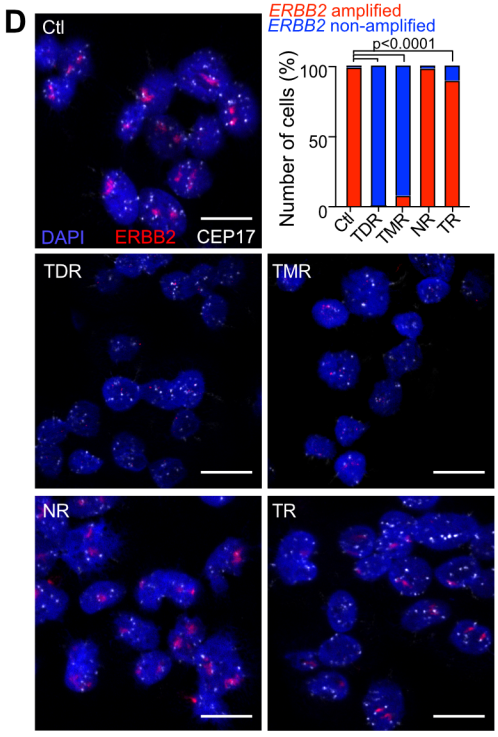

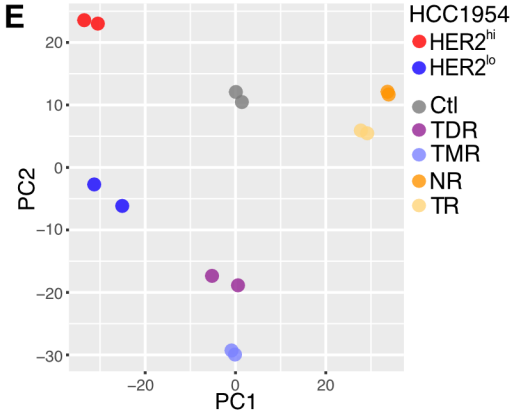

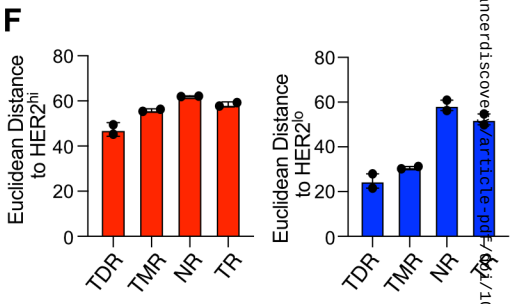

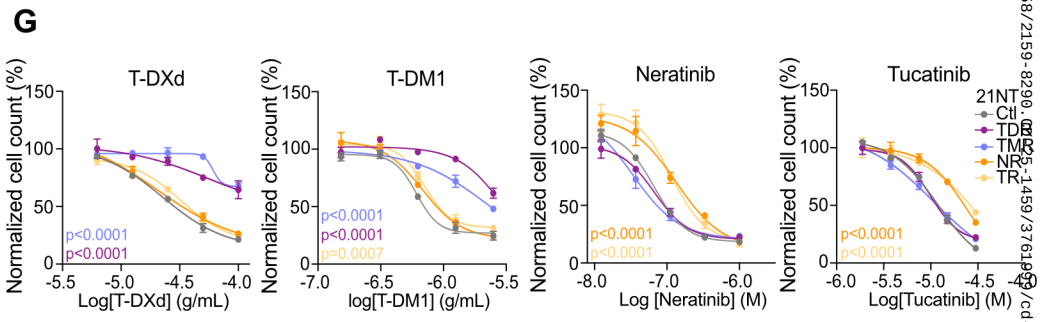

Fig. 3